Robust Trajectory Tracking Control for Underactuated Autonomous Underwater Vehicles in Uncertain Environments

Shahab Heshmati-alamdari, Alexandros Nikou and Dimos V. Dimarogonas

***Abstract*—This paper addresses the tracking control problem of 3D trajectories for underactuated underwater robotic vehicles operating in a constrained workspace including obstacles. More specifically, a robust Nonlinear Model Predictive Control (NMPC) scheme is presented for the case of underactuated Autonomous Underwater Vehicles (AUVs) (i.e., unicycle-like vehicles actuated only in surge, heave and yaw). The purpose of the controller is to steer the unicycle-like AUV to a desired trajectory with guaranteed input and state constraints (e.g., obstacles, predefined vehicle velocity bounds, thruster saturations) inside a partially known and dynamic environment where the knowledge of the operating workspace is constantly updated via the vehicle's on–board sensors. In particular, considering the sensing range of the vehicle, obstacle avoidance with any of the detected obstacles is guaranteed, by on-line generation of a collision-free trajectory tracking path, despite the model dynamic uncertainties and the presence of external disturbances representing ocean currents and waves. Finally, realistic simulation studies verify the performance and efficiency of the proposed framework.**

Note to Practitioners. *This paper was motivated by the problem of robust trajectory tracking for an Autonomous Underwater Vehicle (AUV) operating in an uncertain environment where the knowledge of the operating workspace (e.g. obstacle positions) is constantly updated on–line via the vehicle's on–board sensors (e.g., multi-beam imaging sonars, laser based vision systems). In addition, there may be other system limitations (e.g., thruster saturation limits, etc) and other operational constraints, induced by the need of various common underwater tasks (e.g., a predefined vehicle speed limit for inspecting the seabed, mosaicking etc), where it should also be considered into the control strategy. However, based on the existing trajectory tracking control approaches for underwater robotics, there is a lack of an autonomous control scheme that provides a complete and credible control strategy that takes the aforementioned issues into consideration. Based on the above, we present a reliable control strategy that takes into account the aforementioned issues, along with dynamic uncertainties of the model and the presence of ocean currents. In future research, we will extend the proposed methodology for multiple AUV performing collaborative inspection task in an uncertain environment.*

S. Heshmati-alamdari and D.V. Dimarogonas are with the Division of Decision and Control Systems, School of Electrical Engineering and Computer Science, KTH Royal Institute of Technology, Stockholm SE-10044, Sweden, Email: {shaha, dimos}@kth.se. A. Nikou is with the Ericsson Research, Stockholm, Sweden, E-mail: {alexandros.nikou}@ericsson.com. (Corresponding author: Shahab Heshmati-alamdari). This work was supported by the H2020 ERC Grant BUCOPHSYS, the Swedish Foundation for Strategic Research (SSF), the Swedish Research Council (VR) and the Knut och Alice Wallenberg Foundation (KAW).

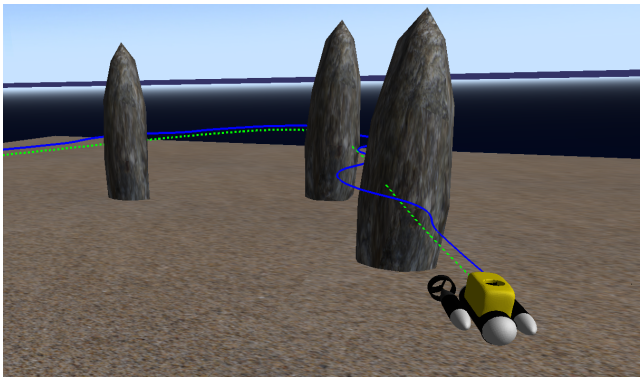

Fig. 1: Trajectory tracking in uncertain and constrained workspace including obstacles where the knowledge of the operating workspace (e.g., the accurate obstacles' positions) is constantly updated via the vehicle's on–board sensors. The reference and actual vehicle trajectories are depicted with green dashed and blue lines respectively.

I. Introduction

During the last decades, considerable progress has been made in the field of unmanned marine vehicles, with a significant number of results in a variety of marine activities [1]. Applications such as ocean forecasting, deep see exploration, underwater inspection of oil/gas pipelines are indicative examples of applications that require the underwater robots to work under various constraints and increased level of autonomy. In particular, Autonomous Underwater Vehicles (AUVs) are characterized by constrained high-dimensional nonlinear dynamics, especially in the case of underactuated systems which induce significant complexity regarding model uncertainty as well as various operational constraints such as sensing capabilities and visibility constraints [2].

A typical marine control problem is trajectory tracking [3]. Classical approaches such as local linearization and input-output decoupling have been used in the past to design motion controllers for underwater vehicles [4]. Nevertheless, the aforementioned methods yielded poor closed-loop performance and the results were local, around only certain selected operating points. Output feedback linearization [5] is an alternative approach which however is not always possible. Moreover, based on a combined approach involving Lyapunov theory and backstepping, various model-based non-linear controllers have been proposed in the literature requiring a very accurate knowledge of the vehicle dynamic parameters, which in most cases is quite difficult to obtain [6]. Moreover, the effect of ocean currents either is assumed to be known or an exponential observer is adopted for its estimation, thus increasing the design complexity [7].

Dynamic model uncertainties of AUVs have been mainly compensated by employing adaptive control techniques [8].

However, the application of these control strategies in a real time experiment is questionable, owing to their sensitivity to unknown parameters. Additionally, based on switching control strategies and backstepping techniques, a hybrid parameter adaptation law was presented in [9], [10]. However, external disturbances and un–modeled dynamics were not considered. Moreover, sliding mode control, owing to its strong robustness against uncertain model and time varying parameters, is an alternative method that has been adopted in order to meet the problem of dynamic model's uncertainties [11]–[13]. Nonetheless, the main disadvantage of the aforementioned control schemes is the inherent control input chattering that is energy intensive and may result in high frequency dynamics, which is undesirable for underwater applications. Finally, adaptive neural network [11], [14], learning [15], [16] and fuzzy control [17], [18] schemes that deal with model uncertainties by exploiting the universal approximation capabilities of neural network and fuzzy system structures, but unfortunately, yield inevitably reduced levels of robustness against modeling imperfections [19].

In addition, by employing all of the aforementioned motion control strategies, it is not always feasible or straightforward to incorporate input (generalized body forces/torques or thrust) and state (3D obstacles, velocities) constraints into the vehicle's closed-loop motion [20]. In that sense, the trajectory control problem of underwater robots continues to pose considerable challenges to system designers, especially in view of the high-demanding missions envisioned by the marine industry (e.g., surveillance of oil platforms, cable tracking, etc.). In this context, Nonlinear Model Predictive Control (NMPC) [21] can be considered a suitable approach for complex underwater missions, as it is able to handle efficiently input and state constraints, while dealing with parameter uncertainties through its robustness [22]. A sampling based Model Predictive Control scheme was proposed in [23] for motion control of underwater vehicles in presence of constraints. A depth control strategy for an over-actuated AUV based on Linear Model Predictive Control was presented in [24]. However, actuator limits were the only considered constraints of the system. In [25], a MPC framework was proposed for the trajectory tracking of a full-actuated AUV under state constraints without taking into account the effects of disturbances and model uncertainties. In the aforementioned studies, the validation of the proposed strategies was conducted via simple simulation tests. Experimental validation of a NMPC scheme for robust stabilization of an AUV was presented in [20].

The reference trajectory for the underwater robot is usually the result of some path planning techniques [26]. The majority of planning techniques are based on off–line optimization schemes, which consider static or quasi–static operational environments. Their output is often a set of way-points or trajectories satisfying certain environmental constraints (i.e., known obstacles). On the other hand, robust AUV control around corals reefs is difficult because of their unstructured dynamic nature. In the absence of GPS in the underwater environment, localization errors are increasing, making any prior knowledge of the environment coarse and inappropriate. Nonetheless, the reference trajectory might not feasible in real ocean environments, due to the fact that ocean is a partially-known environment even in the best case scenario. When operating in such uncertain environment, the underwater vehicle has to be reactive and has the ability to re-calculate its path online in order to generate collision-free paths, as more information about the surroundings becomes available [27].

Motivated by the aforementioned considerations, this article presents a robust trajectory tracking control scheme for underactuated Autonomous Underwater Vehicles (AUVs) operating in a constrained workspace including obstacles. In particular, a robust Nonlinear Model Predictive Control (NMPC) scheme is presented for the underactuated AUVs (i.e., vehicles actuated only in surge, heave and yaw). Various constraints such as: sparse obstacles, workspace boundaries, sensing range capability, predefined upper bounds for the velocity of the underwater robotic vehicle (requirements for several underwater tasks such as seabed inspection scenario, mosaicking etc) as well as thruster saturation are considered during the control design. The purpose of the controller is to steer the underactuated AUV on a desired trajectory inside a constrained and dynamic workspace. Since the knowledge of the operating workspace is constantly updated online via the vehicle's on–board sensors, the robot re-calculates its path online and generates a collision-free trajectory tracking path, if the updated environmental changes (i.e., new detected obstacles) are in conflict with the reference trajectory. In particular, by considering a ball which covers the volume of the system and the sensing range of the vehicle, obstacle avoidance with any of the detected obstacles is guaranteed, by on-line generation of a collision-free trajectory tracking path, despite the model dynamic uncertainties and the presence of external disturbances representing ocean currents and waves. The proposed feedback control law consists of two parts: an online law which is the outcome of a Finite Horizon Optimal Control Problem (FHOCP) solved for the nominal dynamics; and a state feedback law which is tuned off-line and guarantees that the real trajectories remain bounded in a tube centered along the nominal trajectories for all times. The volume of the tube depends on the upper bound of the disturbances as well as bounds of derivatives of the dynamics. The closed-loop system has analytically guaranteed stability and convergence properties.

The rest of the paper is organized as follows. Section II provides the notation and the mathematical preliminaries. The problem treated in the paper in hand is formulated in Section III. Section IV analyzes the proposed framework. In Section V, a simulation study is demonstrated through figures and video. Finally, in section VI conclusions and future research directions are discussed.

II. Notation and Background

The sets of positive integers and real numbers are denoted by $\mathbb{N}$ and $\mathbb{R}$, respectively. $\mathbb{R}^n_{\geq 0}$ and $\mathbb{R}^n_{>0}$ are the sets of real n-vectors with all elements nonnegative and positive, respectively. Given a set $\mathcal{S}$, denote by $|\mathcal{S}|$ and $\mathcal{S}^n := \mathcal{S}\times\cdots\times\mathcal{S}$ its cardinality and its n-fold Cartesian product. Given a vector $\boldsymbol{z} \in \mathbb{R}^n$ define by: $\|\boldsymbol{z}\|_2 := \sqrt{\boldsymbol{z}^\top \boldsymbol{z}}$, $\|\boldsymbol{z}\|_\infty :=$

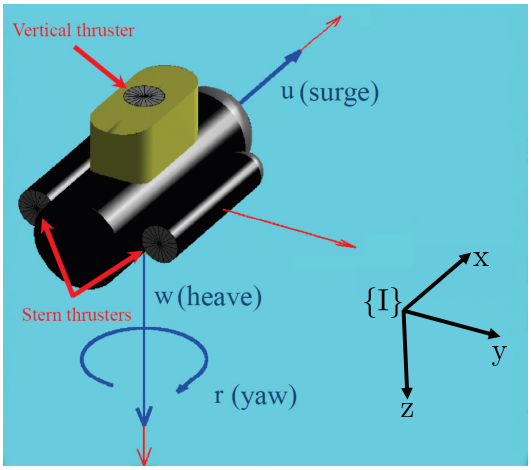

Fig. 2: The underactuated unicycle-like underwater vehicle. Blue color indicates the actuated degrees of freedom.

$\max_{i=1,\dots,n}|\boldsymbol{z}_i|$, $\|\boldsymbol{z}\|_P := \sqrt{\boldsymbol{z}^\top \boldsymbol{P}\boldsymbol{z}}$, its Euclidean, infinite and $\boldsymbol{P}$-weighted norm, respectively, with $\boldsymbol{P} \geq 0$. The notation $\lambda_{\min}(\boldsymbol{P})$ stands for the minimum absolute value of the real part of the eigenvalues of $\boldsymbol{P} \in \mathbb{R}^{n\times n}$; $0_{m\times n} \in \mathbb{R}^{m\times n}$ and $I_n \in \mathbb{R}^{n\times n}$ stand for the $m \times n$ matrix with all entries zeros and the identity matrix, respectively. The notation $\mathrm{diag}\{P_1, \dots, P_n\}$ stands for the block diagonal matrix with the matrices $P_1, \dots, P_n$ in the main diagonal. Moreover $\mathcal{B}(\boldsymbol{c}, r) := \{\boldsymbol{x} \in \mathbb{R}^n : \|\boldsymbol{x} - \boldsymbol{c}\|_2 \leq r\}$, stands for a ball in $\mathbb{R}^n$ with center and radius $\boldsymbol{c} \in \mathbb{R}^n$, $r > 0$, respectively. The boundary of a set A is denoted as ∂A and is defined as $\partial A = A \backslash \mathring{A}$ where $\mathring{A}$ is the interior of set A. Given sets $\mathcal{S}_1$, $\mathcal{Z} \subseteq \mathbb{R}^n$, $\mathcal{S}_2 \subseteq \mathbb{R}^m$ and matrix $\boldsymbol{P} \in \mathbb{R}^{n\times m}$, the *Minkowski addition*, the *Pontryagin difference* and the *matrix-set multiplication* are defined by: $\mathcal{S}_1 \oplus \mathcal{Z} := \{\boldsymbol{s}_1 + \boldsymbol{z} : \boldsymbol{s}_1 \in \mathcal{S}_1, \boldsymbol{z} \in \mathcal{Z}\}$, $\mathcal{S}_1 \ominus \mathcal{Z} := \{\boldsymbol{s}_1 \in \mathcal{S}_1 : \boldsymbol{s}_1 + \boldsymbol{z} \in \mathcal{S}_1, \forall \boldsymbol{z} \in \mathcal{Z}\}$ and $P \circ \mathcal{S}_2 := \{\boldsymbol{P}\boldsymbol{s}, \boldsymbol{s} \in \mathcal{S}_2\}$ respectively.

Definition 1. *[28] Consider a dynamical system:*

$$\dot{\boldsymbol{x}} = f(\boldsymbol{x}, \boldsymbol{u}, \boldsymbol{d}),\ \boldsymbol{x} \in \mathcal{X},\ \boldsymbol{u} \in \mathcal{U},\ \boldsymbol{d} \in \mathcal{D},$$

with initial condition $\boldsymbol{x}(0) \in \mathcal{X}$ and external disturbances $\boldsymbol{d} \in \mathcal{D}$. A set $\mathcal{X}' \subseteq \mathcal{X}$ is a Robust Control Invariant (RCI) set *for the system, if there exists a feedback control law $\boldsymbol{u} := \kappa(\boldsymbol{x}) \in \mathcal{U}$, such that for all $\boldsymbol{x}(0) \in \mathcal{X}'$ and for all $\boldsymbol{d} \in \mathcal{D}$ it holds that $\boldsymbol{x}(t) \in \mathcal{X}'$ for all $t \geq 0$, along every solution $\boldsymbol{x}(t)$ of the closed-loop system.*

Definition 2. *A nonlinear system $\dot{\boldsymbol{x}} = f(\boldsymbol{x}, \boldsymbol{u}, \boldsymbol{d})$, $\boldsymbol{x} \in \mathcal{X}$, $\boldsymbol{u} \in \mathcal{U}$, $\boldsymbol{d} \in \mathcal{D}$, with initial condition $\boldsymbol{x}(0) \in \mathcal{X}$ is said to be* Input-to-State Stable (ISS) *with respect to $\boldsymbol{d} \in \mathcal{D}$, if there exist functions $\beta \in \mathcal{KL}$, $\gamma \in \mathcal{K}$ such that for any initial condition $\boldsymbol{x}(0) \in \mathcal{X}$ and for any input $\boldsymbol{u}(t) \in \mathcal{U}$, the solution $\boldsymbol{x}(t)$ exists for all $t \in \mathbb{R}_{\geq 0}$ and satisfies:*

$$\|\boldsymbol{x}(t)\| \leq \beta\big(\|\boldsymbol{x}(0)\|, t\big) + \gamma\left(\sup_{0\leq \mathfrak{s} \leq t} \|\boldsymbol{d}(\mathfrak{s})\|\right).$$

III. Problem Statement

In this section, the overall problem is formulated. Initially, the mathematical model of the under-actuated underwater vehicle is presented.

A. Mathematical Modeling

The pose vector of the vehicle with respect to (w.r.t.) the inertial frame $\mathcal{I}$ is denoted by $\boldsymbol{\eta}_{\text{tot}} = \left[\boldsymbol{\eta_1^T}\ \boldsymbol{\eta_2^T}\right]^T \in \mathbb{R}^6$ including the position (i.e., $\boldsymbol{\eta_1} = [x\ y\ z]^T$) and orientation (i.e., $\boldsymbol{\eta_2} = [\phi\ \theta\ \psi]^T$) vectors. The $\boldsymbol{v}_{\text{tot}} = \left[\boldsymbol{v_1^T}\ \boldsymbol{v_2^T}\right]^T \in \mathbb{R}^6$ is the velocity vector of the vehicle expressed in body fixed frame $\mathcal{V}$ and includes the linear (i.e., $\boldsymbol{v_1} = [u\ v\ w]^T$) and angular (i.e., $\boldsymbol{v_2} = [p\ q\ r]^T$) velocity vectors (Fig.2). In this work, we consider one of the most common types of underactuated underwater vehicles, namely unicycle-like vehicles (see Fig. 2). The considered unicycle-like vehicles are equipped with a set of thrusters which are effective only in surge, heave and yaw motion (Fig.2), meaning that the vehicle is underactuated along the sway axis.

Remark 1. *The unicycle-like underactuated underwater vehicles considered in this work are usually designed with metacentric restoring forces in order to regulate roll and pitch angles. Thus, the angles ϕ, θ and angular velocities p and q are negligible and we can consider them to be equal to zero [29]. In addition, the vehicle is symmetric about the x - z plane and close to symmetric about the y - z plane. Therefore, we can safely assume that motions in heave, roll and pitch are decoupled [30].*

Without loss of generality and based on the aforementioned considerations, the dynamic equations of the considered underwater robotic vehicle can be given as follows [30]:

$$\dot{x} = u\cos\psi - v\sin\psi \tag{1a}$$
$$\dot{y} = u\sin\psi + v\cos\psi \tag{1b}$$
$$\dot{z} = w \tag{1c}$$
$$\dot{\psi} = r \tag{1d}$$
$$\dot{u} = \frac{1}{m_{11}}\left[m_{22}vr + X_u u + X_{u|u|}|u|u + \tau_X\right] \tag{1e}$$
$$\dot{v} = \frac{1}{m_{22}}\left[-m_{11}ur + Y_v v + Y_{v|v|}|v|v\right] \tag{1f}$$
$$\dot{w} = \frac{1}{m_{33}}\left[(W - B) + Z_w w + Z_{w|w|}|w|w + \tau_Z\right] \tag{1g}$$
$$\dot{r} = \frac{1}{m_{44}}\left[(m_{11} - m_{22})uv + N_r r + N_{r|r|}|r|r + \tau_N\right] \tag{1h}$$

where m_{11} , m_{22}, m_{33}, m_{44} are the terms of the inertia matrix including the added mass, W, B are the vehicle weight and the buoyancy force, X_u, $X_{u|u|}$, Y_v, $Y_{v|v|}$, Z_w, $Z_{w|w|}$, N_r, $N_{r|r|}$ are negative hydrodynamic damping coefficients and τ_X, τ_Z, τ_N are the control inputs of the system and consist of body forces and torque generated by the thrusters along the surge, heave and yaw directions.

Remark 2. *In this work, we consider one of the most common types of underactuated underwater vehicles, namely the*

unicycle-like vehicles (see Fig. 2). In particular, the unicycle-like underactuated vehicles considered in this class are actuated by forces τ_X and τ_Z along the longitudinal (surge) and vertical (heave) axes respectively and a torque τ_N about the vertical (yaw) axis (see Fig. 2). The aforementioned forces τ_X, τ_Z and torque τ_N define the input control variables of the corresponding dynamic system (1)*, which in this case is unactuated in the sway degree of freedom (i.e., $\tau_Y = 0$).*

The dynamic equations of (1) can be re-written as:

$$\dot{\boldsymbol{\eta}} = \boldsymbol{J}(\boldsymbol{\eta})\,\boldsymbol{v} + g(\boldsymbol{\eta}, v) \tag{2a}$$

$$\dot{\boldsymbol{v}} = \boldsymbol{M}^{-1}\Big[\boldsymbol{\tau} + \boldsymbol{C}(\boldsymbol{v}, v)\boldsymbol{v} + \boldsymbol{D}(\boldsymbol{v})\boldsymbol{v} + \boldsymbol{g}\Big] \tag{2b}$$

$$\dot{v} = \frac{1}{m_{22}}\big[-m_{11}ur + Y_v v + Y_{v|v|}|v|v\big]. \tag{2c}$$

where:

- $\boldsymbol{\eta} = [x\ y\ z\ \psi]^\top \in \mathbb{R}^4$ is the pose vector expressed in $\mathcal{I}$;
- $\boldsymbol{v} = [u,\ w,\ r]^\top \in \mathbb{R}^3$ is the velocity vector of the vehicle along actuated degrees of of freedom, expressed in the body fixed frame $\mathcal{V}$;
- $\boldsymbol{\tau} = [\tau_X,\ \tau_Z,\ \tau_N]^\top \in \mathbb{R}^3$ is the propulsion force/torque vector (i.e., the body forces and torques generated by the thrusters) applied on the vehicle and expressed in body-fixed frame $\mathcal{V}$;
- $g(\boldsymbol{\eta}, v) = [-s_\psi,\ c_\psi,\ 0,\ 0]^T v$;
- $\boldsymbol{M} = \mathrm{diag}\big(m_{11}, m_{33}, m_{44}\big) \in \mathbb{R}^{3\times 3}$ is the inertia matrix;
- $\boldsymbol{C}(\boldsymbol{v}, v) = \begin{bmatrix} 0 & 0 & m_{22}v \\ 0 & 0 & 0 \\ (m_{11}-m_{22})v & 0 & 0 \end{bmatrix}$ is the coriolis matrix;
- $\boldsymbol{D}(\boldsymbol{v}) = \begin{bmatrix} X_u + X_{u|u|}|u| & 0 & 0 \\ 0 & Z_w + Z_{w|w|}|w| & 0 \\ 0 & 0 & N_r + N_{r|r|}|r| \end{bmatrix}$ is the drag matrix;
- $\boldsymbol{g} = [0, (W-B),\ 0]^T \in \mathbb{R}^3$ is the hydrostatic restoring force vector;
- $\boldsymbol{J}(\boldsymbol{\eta}) = \begin{bmatrix} \cos(\psi) & 0 & 0 \\ \sin(\psi) & 0 & 0 \\ 0 & 1 & 0 \\ 0 & 0 & 1 \end{bmatrix} \in \mathbb{R}^{4\times 3}$ is the Jacobian matrix transforming the velocities from the body-fixed ($\mathcal{V}$) to the inertial ($\mathcal{I}$) frame;

Notice that the robot moves under the influence of an irrotational current which behaves as an external disturbance on the system's dynamic equation (2b). In particular we set δ_Y and $\boldsymbol{\delta} = [\delta_X, \delta_Z, \delta_N]^\top \in \Delta \subset \mathbb{R}^3$ with Δ being a compact set. In this vein, there exist upper bounds $\bar{\delta}_Y > 0$ and $\bar{\delta} > 0$ such that $|\delta_Y| \leq \bar{\delta}_Y$ and $||\boldsymbol{\delta}|| \leq \bar{\delta}$ respectively. Furthermore, it is assumed that vehicle's dynamic parameters have been identified via a proper identification scheme. However, some degree of model uncertainty should be considered. In particular, we set γ_Y as the model uncertainty regarding the sway direction and $\boldsymbol{\gamma} = [\gamma_X, \gamma_Z, \gamma_N]^\top \in \Gamma \subset \mathbb{R}^3$ as the vector of uncertainties with Γ being a compact set. In the same vein, we assume that there exist positive upper bounds $\bar{\gamma}_Y$ and $\bar{\gamma} \geq 0$, such that $|\gamma_Y| \leq \bar{\gamma}_Y$ and $||\boldsymbol{\gamma}|| \leq \bar{\gamma}$. Taking into consideration the aforementioned disturbances and uncertainties, we can model the perturbed system as follows:

$$\dot{\boldsymbol{\eta}} = \boldsymbol{J}(\boldsymbol{\eta})\,\boldsymbol{v} + g(\boldsymbol{\eta}, v) \tag{3a}$$

$$\dot{\boldsymbol{v}} = \boldsymbol{M}^{-1}\Big[\boldsymbol{\tau} + \boldsymbol{C}(\boldsymbol{v}, v)\boldsymbol{v} + \boldsymbol{D}(\boldsymbol{v})\boldsymbol{v} + \boldsymbol{g}\Big] + \boldsymbol{\xi} \tag{3b}$$

$$\dot{v} = \frac{1}{m_{22}}\big[-m_{11}ur + Y_v v + Y_{v|v|}|v|v\big] + \delta_Y. \tag{3c}$$

where $\boldsymbol{\xi} = \boldsymbol{\gamma} + \boldsymbol{\delta} \in \Xi \subset \mathbb{R}^3$ in the vector that is the result of adding uncertainties and external disturbances and Ξ is a compact set with $\Xi = \Delta \oplus \Gamma$. Since the sets Δ and Γ are compact, we have that Ξ is also compact, and:

$$\Xi := \{\boldsymbol{\xi}(t) \in \mathbb{R}^3 : ||\boldsymbol{\xi}(t)||_2 \leq \bar{\xi}\} \tag{4}$$

with $\bar{\xi} \triangleq \bar{\delta} + \bar{\gamma}$.

B. Geometry of the Workspace

We consider that the underwater vehicle operates inside a workspace $\mathcal{W} \subset \mathbb{R}^3$ with boundary $\partial\mathcal{W}$ and scattered obstacles located within it. Without loss of the generality, the robot and the obstacles are modeled by spheres (i.e., we adopt the spherical world representation [31]). Let $\mathcal{B}(\boldsymbol{\eta}_1, \tilde{r})$ be a closed ball that covers the whole vehicle volume (main body and additional equipments). Moreover, let $\mathcal{B}(\boldsymbol{\eta}_1, \bar{R})$ with $\bar{R} > \tilde{r}$ be a sensing area where the robot can perceive and update its knowledge of the workspace (i.e., the obstacle locations) using its on-board sensors. Furthermore, the $\mathcal{M}$ static obstacles within the workspace are defined as closed balls described by $\pi_m = \mathcal{B}(\boldsymbol{p}_{\pi_m}, r_{\pi_m}),\ m \in \{1, \ldots, \mathcal{M}\}$, where $\boldsymbol{p}_{\pi_m} \in \mathbb{R}^3$ is the center and $r_{\pi_m} > 0$ the radius of the obstacle π_m. Additionally, based on the property of spherical world [31], for each pair of obstacles m, m' with $m \neq m'$ we have: $||\pi_m - \pi_{m'}|| > 2\tilde{r} + r_{\pi_m} + r_{\pi'_m}$, which intuitively means that the obstacles m and m' are disjoint in such a way that the entire volume of the vehicle can pass through the free space between them. Therefore, there exists a feasible trajectory $\boldsymbol{\eta}_1(t)$ for the vehicle such that:

$$\mathcal{B}(\boldsymbol{\eta}_1(t), \tilde{r}) \cap \{\mathcal{B}(\boldsymbol{p}_{\pi_m}, r_{\pi_m}) \cup \partial\mathcal{W}\} = \emptyset, \quad \forall t \geq 0, m \in \{1, \ldots, \mathcal{M}\} \tag{5}$$

A graphical representation of the feasible trajectory is depicted in Fig. 3.

C. Constraints

1) State Constraints: as already stated, the robot should be able to avoid the newly detected obstacles which may had been unknown to the off-line trajectory planner. Moreover, for the needs of several common underwater tasks (e.g., seabed inspection, mosaicking), the vehicle is required to move with relatively low speeds with upper bound denoted by $\bar{v}$ and the velocity vector $\bar{\boldsymbol{v}} = [\bar{u}\ \bar{w}\ \bar{r}]^\top$, where $(\bar{\cdot})$ denotes the corresponding upper bounds for each coefficient. These requirements are captured by the state constraint sets H and V, given by:

$$\boldsymbol{\eta}(t) \in H \subset \mathbb{R}^4, \quad \text{and} \quad \boldsymbol{v}(t) \in V \subset \mathbb{R}^3 \tag{6}$$

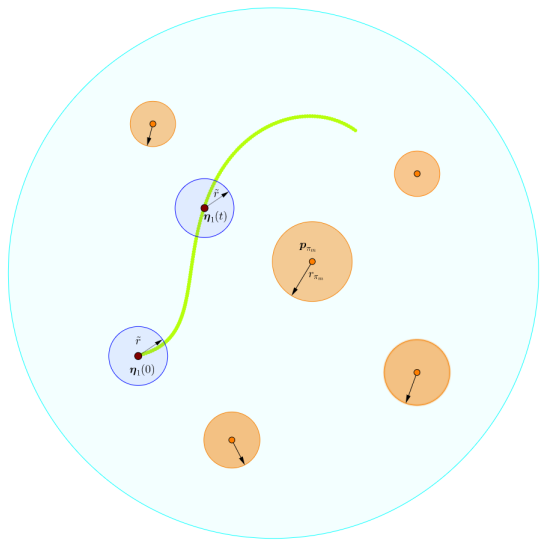

Fig. 3: Graphical representation of a feasible trajectory in the workspace. The boundary of workspace $\partial\mathcal{W}$ is illustrated in cyan. The orange areas indicate the obstacles within the workspace $\mathcal{W}$. The blue line encircles the area covered by the vehicle at times 0 and t with $t > 0$ respectively. The feasible trajectory of the vehicle is depicted in green.

which can be defined as:

$$V := \left\{ \boldsymbol{v} \in \mathbb{R}^3 : |u| \leq \bar{u},\ |w| \leq \bar{w},\ |r| \leq \bar{r} \right\} \tag{7}$$

with upper bound as $\bar{V} = (\bar{u} + \bar{w} + \bar{r})^{\frac{1}{2}}$, and

$$H := \Big\{ \boldsymbol{\eta} \in \mathbb{R}^4 : \mathcal{B}(\boldsymbol{\eta}_1, \tilde{r}) \cap \{\mathcal{B}(\boldsymbol{p}_{\pi_m}, r_{\pi_m}) \cup \partial\mathcal{W}\} = \emptyset, \\ m \in \{1, \ldots, \mathcal{M}\} \Big\} \tag{8}$$

2) Input Constraints: The actuation body forces and torques are generated by the thrusters. Thus, we define the control constraint set T as follows:

$$\boldsymbol{\tau}(t) = [\tau_X,\ \tau_Z,\ \tau_N]^\top \in T \subseteq \mathbb{R}^3 \tag{9}$$

which can be defined as:

$$T := \left\{ \boldsymbol{\tau} \in \mathbb{R}^3 : |\tau_X| \leq \bar{\tau}_X, |\tau_Z| \leq \bar{\tau}_Z, |\tau_N| \leq \bar{\tau}_N \right\} \tag{10}$$

with $\bar{\tau}_X, \bar{\tau}_Z, \bar{\tau}_N \in \mathbb{R}_{\geq 0}$ are the corresponding upper bound for each thrust directions.

D. Problem statement

Let $\boldsymbol{p}_d(t) = [x_d(t), y_d(t), z_d(t)]^T$ denote a smooth desired trajectory with bounded time derivatives, thus, the problem of this paper can be stated as follows:

Problem 1. *(Robust Tracking Control for an Autonomous Underactuated Underwater Vehicle): Consider an Underactuated Autonomous Underwater Vehicle described by* (3) *operating in a workspace $\mathcal{W} \subset \mathbb{R}^3$ with state and input constraints as well as disturbances imposed by the sets H, V and T as well as Ξ as in* (6), (9) *and* (4), *respectively. Consider also that the robot and the obstacles are all modeled according to the spherical world representation*[1] *and the knowledge of the operating workspace $\mathcal{W}$ (e.g., obstacles positions) is constantly updated via the vehicle's on–board sensors inside a sensing region defined by $\mathcal{B}(\boldsymbol{\eta}_1, \bar{R})$. Given a desired trajectory $\boldsymbol{p}_d(t) = [x_d(t), y_d(t), z_d(t)]^T$, design a feedback control law $\boldsymbol{\tau} = \kappa(\boldsymbol{\eta}, \boldsymbol{v}) \in T$ such that the desired trajectory $\boldsymbol{p}_d(t)$ is tracked, while guaranteeing the following specifications:*

- *Capability to be flexible regarding environmental changes (i.e., avoiding new detected obstacles which may coincide with desired trajectory, etc.)*
- *Respect operational limitations in the form of state (e.g velocity bounds) and input (thrust saturation) constraints:*

$$\boldsymbol{\eta}(t) \in H, \quad \boldsymbol{v}(t) \in V, \quad \boldsymbol{\tau}(t) \in T.$$

- *Respect capability sensing range of the system.*
- *Predefined robustness with respect to the external disturbances and model uncertainties*

[1]as described in section-III-B

IV. Methodology

In this section we present in detail the methodology proposed in order to formulate the solution of Problem-1 defined in Section-III-D. In particular, a Nonlinear Model Predictive Control (NMPC) framework [32]–[35] is utilized, and a relevant robust NMPC analysis, the so-called tube-based approach is provided here for the trajectory tracking problem for underactuated systems in presence of disturbances. The proposed feedback control law consists of two parts: an on-line control law which is the outcome of Finite Horizon Optimal Control Problem (FHOCP) for the nominal system dynamics and a state feedback law which guarantees that the real system trajectories always lie within a tube centered along the nominal trajectories. First we begin by defining the error states and the corresponding transformed constraints.

A. Error Definitions

Given the desired trajectory $\boldsymbol{p}_d(t) = [x_d(t), y_d(t), z_d(t)]^T$, let us define the position errors:

$$e_x(t) = x - x_d(t),\ e_y(t) = y - y_d(t),\ e_z(t) = z - z_d(t) \tag{11}$$

the projected on the horizontal plane distance error:

$$e_d(t) = \sqrt{e_x^2(t) + e_y^2(t)} \tag{12}$$

as well as the projected on the horizontal plane orientation error:

$$e_o(t) = \frac{e_y(t)}{e_d(t)} c_{\psi(t)} - \frac{e_x(t)}{e_d(t)} s_{\psi(t)} = s_{\psi_e} \tag{13}$$

where $s_\star = \sin(\star)$, $c_\star = \cos(\star)$, ψ is the yaw angle and ψ_e is the angle measured from the normalized error vector

$$\boldsymbol{e}_d = \left[\frac{e_x}{e_d},\ \frac{e_y}{e_d},\ 0 \right]^\top,$$

on the horizontal plane to the normalized projection of the longitudinal axis of the vehicle on the horizontal plane, defined by the vector $[c_\psi, s_\psi, 0]^\top$ (See Fig. 4). Now, differentiating

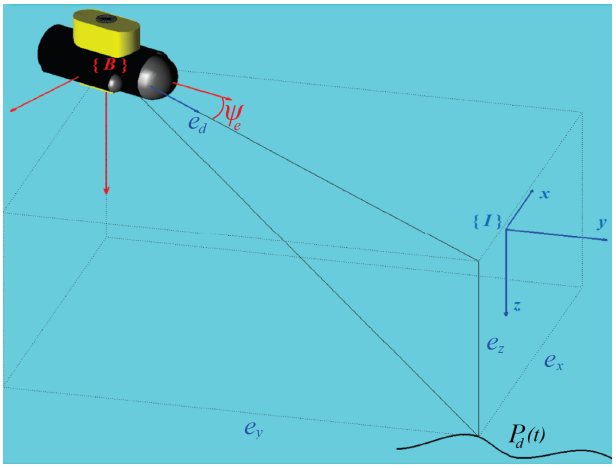

Fig. 4: Graphical illustration of the error definition.

the aforementioned errors of (11)-(13) and employing (2), and using the:

$$c_{\psi_e} = \frac{e_x}{e_d}c_\psi + \frac{e_y}{e_d}s_\psi$$
$$c_{\psi+\psi_e} = c_\psi c_{\psi_e} - s_\psi s_{\psi_e} = \frac{e_x}{e_d}$$
$$s_{\psi+\psi_e} = s_\psi c_{\psi_e} + c_\psi s_{\psi_e} = \frac{e_y}{e_d}$$

we arrive at:

$$\dot{e}_d = c_{\psi_e}u - \dot{x}_d c_{\psi+\psi_e} - \dot{y}_d s_{\psi+\psi_e} + s_{\psi_e}v \tag{14}$$

$$\dot{e}_z = \dot{z} - \dot{z}_d \Rightarrow \dot{e}_z = w - \dot{z}_d \tag{15}$$

$$\dot{e}_o = -\frac{s_{\psi_e}c_{\psi_e}}{e_d}u - c_{\psi_e}r + \frac{\dot{x}_d}{e_d}\left[s_{\psi_e}c_{\psi+\psi_e} + s_\psi\right] + \frac{\dot{y}_d}{e_d}\left[s_{\psi_e}s_{\psi+\psi_e} - c_\psi\right] + \frac{c^2_{\psi_e}}{e_d}v \tag{16}$$

By defining the error vector $\boldsymbol{e} = [e_d,\ e_z,\ e_o]^\top$, the aforementioned formulas can be written in matrix form as:

$$\dot{\boldsymbol{e}} = J(\boldsymbol{e}, \boldsymbol{p}_d)\boldsymbol{v} + \zeta(\boldsymbol{e}, \dot{\boldsymbol{p}}_d) + \xi(\boldsymbol{e}, v) \tag{17}$$

where:

$$J(\boldsymbol{e}, \boldsymbol{p}_d) := \begin{bmatrix} c_{\psi_e} & 0 & 0 \\ 0 & 1 & 0 \\ -\frac{s_{\psi_e}c_{\psi_e}}{e_d} & 0 & -c_{\psi_e} \end{bmatrix},\ \xi(\boldsymbol{e}, v) := \begin{bmatrix} s_{\psi_e}v \\ 0 \\ \frac{c^2_{\psi_e}}{e_d}v \end{bmatrix}$$

$$\zeta(\boldsymbol{e}, \dot{\boldsymbol{p}}_d) := \begin{bmatrix} -\dot{x}_d c_{\psi-\psi_e} - \dot{y}_d s_{\psi-\psi_e} \\ -\dot{z}_d \\ \frac{\dot{x}_d}{e_d}\left[s_{\psi_e}c_{\psi+\psi_e} + s_\psi\right] + \frac{\dot{y}_d}{e_d}\left[s_{\psi_e}s_{\psi+\psi_e} - c_\psi\right] \end{bmatrix}$$

which are the transformed kinematic error equations of the underwater vehicle system. It should be noted that the tracking control problem is solved if the projected on the horizontal plane distance error e_d, the vertical error e_z and the orientation error e_o converge to zero. Moreover it should be noticed that the orientation error e_o as well as the Jacobian matrix $J(\boldsymbol{e}, \boldsymbol{p}_d)$ are well-defined when the following holds:

$$e_d(t) > 0 \text{ and } -\frac{\pi}{2} < \psi_e < \frac{\pi}{2},\ \forall t \geq 0. \tag{18}$$

Thus, a feasible error configuration imposed to the system is captured by the set:

$$\mathcal{E} := \left\{\boldsymbol{\eta} \in H : \sqrt{e_x^2 + e_y^2} \geq \epsilon_d,\ \ -\frac{\pi}{2} + \epsilon_r \leq \psi_e \leq \frac{\pi}{2} - \epsilon_r\right\}. \tag{19}$$

where ϵ_d and ϵ_o are arbitrarily small positive constants, that guarantee avoidance of the aforementioned singularity issues.

Remark 3. *It should be noted that in $J(\boldsymbol{e}, \boldsymbol{p}_d)$, the singularity appears when $\det(J(\boldsymbol{e}, \boldsymbol{p}_d)) = -|\cos(\psi_e)|^2 = 0 \implies |\psi_e| = \frac{\pi}{2}$. On the other hand, we have that the angle ψ_e is the pointing angle of the vehicle to the target trajectory. Therefore, a configuration where $|\psi_e| > \pi/2$ will not be singular, but the vehicle in this case will face the desired trajectory from the opposite side. In this respect, we select and impose the feasible error configuration set in* (19)*, in order to guarantee that i) the system is in a non-singular configuration as well as that ii) the vehicle is facing directly the target trajectory.*

Remark 4. *It should be noted that the constraint set $\mathcal{E}$ in* (19) *guarantees that $\boldsymbol{J}(\boldsymbol{e}, \boldsymbol{p}_d)$ is non-singular. Thus, there exists strictly positive constants $\underline{J}$ and $\bar{J}$ such that:*

$$\lambda_{\min}\left(\frac{J(\cdot) + J^\top(\cdot)}{2}\right) \geq \underline{J} > 0 \text{ and } \|J(\cdot)\| \leq \bar{J},$$

respectively.

Now, in view of (17) and considering the perturbed dynamic equations of (3a)-(3c), the uncertain transformed kinematics/dynamics of the systems can be given as follows:

$$\dot{\boldsymbol{e}} = J(\boldsymbol{e}, \boldsymbol{p}_d)\boldsymbol{v} + \zeta(\boldsymbol{e}, \dot{\boldsymbol{p}}_d) + \xi(\boldsymbol{e}, v) \tag{20a}$$
$$\dot{\boldsymbol{v}} = \boldsymbol{M}^{-1}\left[\boldsymbol{\tau} + \boldsymbol{C}(\boldsymbol{v}, v)\boldsymbol{v} + \boldsymbol{D}(\boldsymbol{v})\boldsymbol{v} + \boldsymbol{g}\right] + \boldsymbol{\xi} \tag{20b}$$
$$\dot{v} = \frac{1}{m_{22}}\left[-m_{11}ur + Y_v v + Y_{v|v|}|v|v\right] + \delta_Y \tag{20c}$$

The corresponding nominal dynamics (i.e., $\boldsymbol{\xi} = \boldsymbol{0}$) are now given by:

$$\dot{\hat{\boldsymbol{e}}} = J(\hat{\boldsymbol{e}}, \boldsymbol{p}_d)\hat{\boldsymbol{v}} + \zeta(\hat{\boldsymbol{e}}, \dot{\boldsymbol{p}}_d) + \xi(\hat{\boldsymbol{e}}, \hat{v}) \tag{21a}$$
$$\dot{\hat{\boldsymbol{v}}} = \boldsymbol{M}^{-1}\left[\hat{\boldsymbol{\tau}} + \boldsymbol{C}(\hat{\boldsymbol{v}}, \hat{v})\hat{\boldsymbol{v}} + \boldsymbol{D}(\hat{\boldsymbol{v}})\hat{\boldsymbol{v}} + \boldsymbol{g}\right] \tag{21b}$$
$$\dot{\hat{v}} = \frac{1}{m_{22}}\left[-m_{11}\hat{u}\hat{r} + Y_v\hat{v} + Y_{v|v|}|\hat{v}|\hat{v}\right] \tag{21c}$$

It should be noticed that we use the $(\hat{\cdot})$ notation for the nominal state in order to account for the mismatch between the real state and the nominal one which will be used in the following analysis.

B. State Feedback Design

Consider the feedback law:

$$\boldsymbol{\tau} = \hat{\boldsymbol{\tau}}(\hat{\boldsymbol{e}}, \hat{\boldsymbol{v}}) + \kappa(\boldsymbol{e}, \hat{\boldsymbol{e}}, \boldsymbol{v}, \hat{\boldsymbol{v}}) \tag{22}$$

which consists of a nominal control action $\hat{\boldsymbol{\tau}}(\hat{\boldsymbol{e}}, \hat{\boldsymbol{v}}) \in T$ and a state feedback law $\kappa : \mathbb{R}^3 \times \mathbb{R}^3 \to T$. The control action $\hat{\boldsymbol{\tau}}(\hat{\boldsymbol{e}}, \hat{\boldsymbol{v}})$ will be the outcome of a FHOCP solved for the nominal dynamics (21) while the state feedback law $\kappa(\cdot)$ is designed in order to guarantee that the real trajectories $\boldsymbol{e}(t)$, $\boldsymbol{v}(t)$ (i.e., the solution of (20)) always remain inside a bounded tube centered along the nominal trajectories $\hat{\boldsymbol{e}}(t)$, $\hat{\boldsymbol{v}}(t)$ i.e.,

the solution of (21). Now let us define by $\boldsymbol{\rho}_e(t)$ and $\boldsymbol{\rho}_v(t)$ the discrepancy between the real errors and the nominal ones, given as:

$$\boldsymbol{\rho}_e(t) := \boldsymbol{e}(t) - \hat{\boldsymbol{e}}(t) \tag{23a}$$
$$\boldsymbol{\rho}_v(t) := \boldsymbol{v}(t) - \hat{\boldsymbol{v}}(t) \tag{23b}$$

with $\boldsymbol{\rho}_e(0) = \boldsymbol{e}(0) - \hat{\boldsymbol{e}}(0) = \mathbf{0}$ and $\boldsymbol{\rho}_v(0) = \boldsymbol{e}(0) - \hat{\boldsymbol{e}}(0) = \mathbf{0}$ respectively. In view of (23a), the dynamics of $\boldsymbol{\rho}_e(t)$ are given as:

$$\begin{aligned}\dot{\boldsymbol{\rho}}_e &= \dot{\boldsymbol{e}} - \dot{\hat{\boldsymbol{e}}} \\ &= J(\boldsymbol{e}, \boldsymbol{p}_d)\boldsymbol{v} - J(\hat{\boldsymbol{e}}, \boldsymbol{p}_d)\hat{\boldsymbol{v}} + \zeta(\boldsymbol{e}, \dot{\boldsymbol{p}}_d) - \zeta(\hat{\boldsymbol{e}}, \dot{\boldsymbol{p}}_d) \\ &\quad + \xi(\boldsymbol{e}, v) - \xi(\hat{\boldsymbol{e}}, \hat{v}).\end{aligned} \tag{24}$$

By adding and subtracting the term $J(\boldsymbol{e}, \boldsymbol{p}_d)\hat{\boldsymbol{v}}$ and by defining the function

$$h_e(\boldsymbol{e}, \hat{\boldsymbol{v}}) := J(\boldsymbol{e}, \boldsymbol{p}_d)\hat{\boldsymbol{v}},$$

for which it also holds that:

$$h_e(\hat{\boldsymbol{e}}, \hat{\boldsymbol{v}}) := J(\hat{\boldsymbol{e}}, \boldsymbol{p}_d)\hat{\boldsymbol{v}},$$

(24) becomes:

$$\begin{aligned}\dot{\boldsymbol{\rho}}_e = h_e(\boldsymbol{e}, \hat{\boldsymbol{v}}) - h_e(\hat{\boldsymbol{e}}, \hat{\boldsymbol{v}}) + J(\boldsymbol{e}, \boldsymbol{p}_d)\boldsymbol{\rho}_v + \zeta(\boldsymbol{e}, \dot{\boldsymbol{p}}_d) - \zeta(\hat{\boldsymbol{e}}, \dot{\boldsymbol{p}}_d) \\ + \xi(\boldsymbol{e}, v) - \xi(\hat{\boldsymbol{e}}, \hat{v}).\end{aligned} \tag{25}$$

Note that for the continuously differentiable functions $h_e(\cdot)$, $\zeta(\cdot)$ and $\xi(\cdot)$ the following hold:

$$\|h_e(\boldsymbol{e}, \hat{\boldsymbol{v}}) - h_e(\hat{\boldsymbol{e}}, \hat{\boldsymbol{v}})\| \leq \mathcal{L}_1\|\boldsymbol{e} - \hat{\boldsymbol{e}}\| = \mathcal{L}_1\|\boldsymbol{\rho}_e\|, \tag{26a}$$
$$\|\zeta(\boldsymbol{e}, \dot{\boldsymbol{p}}_d) - \zeta(\hat{\boldsymbol{e}}, \dot{\boldsymbol{p}}_d)\| \leq \mathcal{L}_2\|\boldsymbol{e} - \hat{\boldsymbol{e}}\| = \mathcal{L}_2\|\boldsymbol{\rho}_e\|, \tag{26b}$$
$$\begin{aligned}\|\xi(\boldsymbol{e}, v) - \xi(\hat{\boldsymbol{e}}, \hat{v})\| &\leq \mathcal{L}_3\|\boldsymbol{e} - \hat{\boldsymbol{e}}\| + \mathcal{L}_4\|v - \hat{v}\|, \\ &= \mathcal{L}_3\|\boldsymbol{\rho}_e\| + \mathcal{L}_4\|v - \hat{v}\|,\end{aligned} \tag{26c}$$

where $\mathcal{L}_1$, $\mathcal{L}_2$, $\mathcal{L}_3$, $\mathcal{L}_4 > 0$ stand for their Lipschitz constants.

The time derivative of the signal $\boldsymbol{\rho}_v$ in view of (23b) is given as:

$$\dot{\boldsymbol{\rho}}_v = \dot{\boldsymbol{v}} - \dot{\hat{\boldsymbol{v}}} = \boldsymbol{M}^{-1}(\boldsymbol{\tau} - \hat{\boldsymbol{\tau}}) + \varphi(\boldsymbol{v}, v) - \varphi(\hat{\boldsymbol{v}}, \hat{v}) + \boldsymbol{\xi}, \tag{27}$$

where for the continuously differentiable function

$$\begin{aligned}\varphi(\boldsymbol{v}, v) &:= \boldsymbol{M}^{-1}\big[\boldsymbol{C}(\boldsymbol{v}, v)\boldsymbol{v} + \boldsymbol{D}(\boldsymbol{v})\boldsymbol{v} + \boldsymbol{g}\big], \\ \varphi(\hat{\boldsymbol{v}}, \hat{v}) &:= \boldsymbol{M}^{-1}\big[\boldsymbol{C}(\hat{\boldsymbol{v}}, \hat{v})\hat{\boldsymbol{v}} + \boldsymbol{D}(\boldsymbol{v}, \hat{v})\hat{\boldsymbol{v}} + \boldsymbol{g}\big],\end{aligned}$$

it holds that:

$$\begin{aligned}\|\varphi(\boldsymbol{v}, v) - \varphi(\hat{\boldsymbol{v}}, \hat{v})\| &\leq \mathcal{L}_5\|\boldsymbol{v} - \hat{\boldsymbol{v}}\| + \mathcal{L}_6\|v - \hat{v}\| \\ &= \mathcal{L}_5\|\boldsymbol{\rho}_v\| + \mathcal{L}_6\|v - \hat{v}\|.\end{aligned} \tag{28}$$

It will be proven thereafter that for the unactuated velocities v, $\hat{v}$ it holds that:

$$\|v - \hat{v}\| \leq \bar{v} + \hat{\bar{v}}, \tag{29}$$

where $\bar{v}$ and $\hat{\bar{v}}$ to be defined Section IV-C. Now based on the aforementioned analysis the following Lemma can be stated:

Lemma 1. *The state feedback law:*

$$\kappa(\boldsymbol{e}, \hat{\boldsymbol{e}}, \boldsymbol{v}, \hat{\boldsymbol{v}}) := -k\sigma(\boldsymbol{e} - \hat{\boldsymbol{e}}) - \sigma(\boldsymbol{v} - \hat{\boldsymbol{v}}), \tag{30}$$

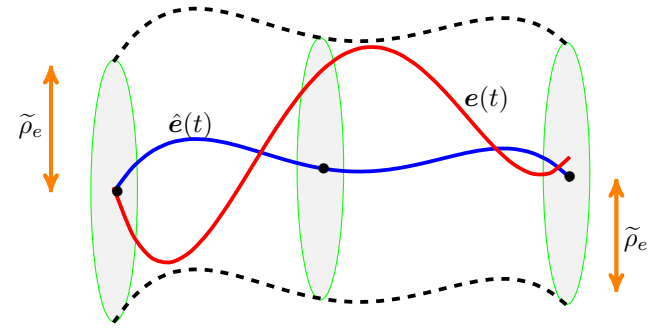

Fig. 5: The tube centered along the trajectory $\hat{\boldsymbol{e}}(t)$ (depicted by the blue line) with radius $\widetilde{\rho}_e$. Under the proposed control law, the real trajectory $\boldsymbol{e}(t)$ (depicted with red line) lies inside the tube for all times, i.e., $\|\boldsymbol{\rho}_e(t)\| \leq \widetilde{\rho}_e$, $\forall t \in \mathbb{R}_{\geq 0}$.

where the gains are chosen such that:

$$k := \frac{\mathcal{L} + \underline{k} + \mathcal{L}_4(\bar{v} + \hat{\bar{v}})}{\lambda_{\min}(J)}, \quad \underline{k} > 0, \quad \varpi > \frac{\alpha_1}{4\underline{k}}, \quad \sigma > \frac{\alpha_1\varpi + \alpha_2}{\lambda_{\min}(\boldsymbol{M}^{-1})} \tag{31a}$$

$$\alpha_1 := \mathcal{L} + k\mathcal{L}_5 + k\mathcal{L}_6(\bar{v} + \hat{\bar{v}}), \quad \alpha_2 := \mathcal{L}_5 + \mathcal{L}_6(\bar{v} + \hat{\bar{v}}) + \bar{J}, \tag{31b}$$

renders the sets:

$$\mathcal{Z}_1 = \left\{\boldsymbol{\rho}_e : \|\boldsymbol{\rho}_e\| \leq \widetilde{\rho}_e := \frac{\bar{\xi}}{\min\{\varsigma_1, \varsigma_2\}}\right\}, \tag{32a}$$
$$\mathcal{Z}_2 = \left\{\boldsymbol{\rho}_v : \|\boldsymbol{\rho}_v\| \leq \widetilde{\rho}_v := \frac{(1+k)\bar{\xi}}{\min\{\varsigma_1, \varsigma_2\}}\right\}, \tag{32b}$$

RCI sets for the error dynamics (25) *and* (27)*, where the constants* ς_1, ς_2 *are given by:*

$$\varsigma_1 := \underline{k} - \frac{\alpha_1}{4\varpi} > 0, \quad \varsigma_2 := \sigma\lambda_{\min}(\boldsymbol{M}^{-1}) - \alpha_1\varpi - \alpha_2 > 0. \tag{33}$$

Proof. A baskstepping control design technique will be adopted. The signal $\boldsymbol{\rho}_e$ in (25) can be seen as the virtual control input to be designed in ordered to stabilize the system (25). Consider the positive definite function $\Lambda_1(\boldsymbol{\rho}_e) = \frac{1}{2}\|\boldsymbol{\rho}_e\|^2$. The time derivative of Λ_1 along the solutions of system (25) is given by:

$$\begin{aligned}\dot{\Lambda}_1(\boldsymbol{\rho}_e) &= \boldsymbol{\rho}_e^\top[h(\boldsymbol{e}, \boldsymbol{v}) - h(\hat{\boldsymbol{e}}, \hat{\boldsymbol{v}})] + \boldsymbol{\rho}_e^\top[\zeta(\boldsymbol{e}, \dot{\boldsymbol{p}}_d) - \zeta(\hat{\boldsymbol{e}}, \dot{\boldsymbol{p}}_d)] \\ &\quad + \boldsymbol{\rho}_e^\top J(\boldsymbol{e}, \boldsymbol{p}_d)\boldsymbol{\rho}_v + \boldsymbol{\rho}_e^\top[\,\xi(\boldsymbol{e}, v) - \xi(\hat{\boldsymbol{e}}, \hat{v})] \\ &\leq \mathcal{L}_1\|\boldsymbol{\rho}_e\|^2 + \mathcal{L}_2\|\boldsymbol{\rho}_e\|^2 + \boldsymbol{\rho}_e^\top J(\boldsymbol{e}, \boldsymbol{p}_d)\boldsymbol{\rho}_v \\ &\quad + \mathcal{L}_3\|\boldsymbol{\rho}_e\|^2 + \mathcal{L}_4(\bar{v} + \hat{\bar{v}}) \\ &= \mathcal{L}\|\boldsymbol{\rho}_e\|^2 + \boldsymbol{\rho}_e^\top J(\boldsymbol{e}, \boldsymbol{p}_d)\boldsymbol{\rho}_v + \mathcal{L}_4(\bar{v} + \hat{\bar{v}}),\end{aligned}$$

where $\mathcal{L} := \mathcal{L}_1 + \mathcal{L}_2 + \mathcal{L}_3$. By designing the virtual control input as $\boldsymbol{\rho}_v = -k\boldsymbol{\rho}_e$ where $k := \frac{\mathcal{L} + \underline{k} + \mathcal{L}_4(\bar{v} + \hat{\bar{v}})}{\lambda_{\min}(J)}$, $\underline{k} > 0$ it holds that:

$$\begin{aligned}\dot{\Lambda}_1(\boldsymbol{\rho}_e) &\leq \mathcal{L}\|\boldsymbol{\rho}_e\|^2 - k\boldsymbol{\rho}_e^\top J(\boldsymbol{e}, \boldsymbol{p}_d)\boldsymbol{\rho}_e + \mathcal{L}_4(\bar{v} + \hat{\bar{v}}) \\ &\leq \mathcal{L}\|\boldsymbol{\rho}_e\|^2 - k\lambda_{\min}(J)\|\boldsymbol{\rho}_e\|^2 + \mathcal{L}_4(\bar{v} + \hat{\bar{v}}) \\ &= -\left[k\lambda_{\min}(J) - \mathcal{L}\right]\|\boldsymbol{\rho}_e\|^2 + \mathcal{L}_4(\bar{v} + \hat{\bar{v}}) \\ &= -\underline{k}\|\boldsymbol{\rho}_e\|^2 + \mathcal{L}_4(\bar{v} + \hat{\bar{v}}).\end{aligned}$$

By taking the aforementioned virtual control design into consideration, define the backstepping auxiliary vector by:

$$\boldsymbol{\varrho} := \boldsymbol{\rho}_v + k\boldsymbol{\rho}_e, \quad \mathfrak{n} := [\boldsymbol{\rho}_e^\top, \boldsymbol{\varrho}^\top]^\top.$$

and consider the function $\Lambda(\mathfrak{n}) := \frac{1}{2}\|\mathfrak{n}\|^2$. Then, the time derivative of $\Lambda(\mathfrak{n})$ is given by:

$$\begin{aligned}\dot{\Lambda}(\mathfrak{n}) &= \boldsymbol{\rho}_e^\top \dot{\boldsymbol{\rho}}_e + \boldsymbol{\varrho}^\top \dot{\boldsymbol{\varrho}} \\ &= \boldsymbol{\rho}_e^\top \dot{\boldsymbol{\rho}}_e + \boldsymbol{\varrho}^\top [\dot{\boldsymbol{\rho}}_v + k\dot{\boldsymbol{\rho}}_e] \\ &= [\boldsymbol{\rho}_e + k\boldsymbol{\varrho}]^\top \dot{\boldsymbol{\rho}}_e + \boldsymbol{\varrho}^\top [\varphi(\boldsymbol{v}, v) - \varphi(\hat{\boldsymbol{v}}, \hat{v})] \\ &\quad + \boldsymbol{\varrho}^\top \boldsymbol{M}^{-1}(\boldsymbol{\tau} - \hat{\boldsymbol{\tau}}) + \boldsymbol{\varrho}^\top \boldsymbol{\xi} \end{aligned} \tag{34}$$

By using the fact that:

$$xy \leq \frac{1}{\varpi}x^2 + \varpi y^2,$$

for every x, $y \in \mathbb{R}$, $\varpi > 0$, we get:

$$\|\boldsymbol{\rho}_e\|\|\boldsymbol{\varrho}\| \leq \frac{1}{4\varpi}\|\boldsymbol{\rho}_e\|^2 + \varpi\|\boldsymbol{\varrho}\|^2.$$

By using the latter, (34) becomes:

$$\begin{aligned}\dot{\Lambda}(\mathfrak{n}) \leq &-\left(\underline{k} - \frac{\alpha_1}{4\varpi}\right)\|\boldsymbol{\rho}_e\|^2 + (\alpha_1\varpi + \alpha_2)\|\boldsymbol{\varrho}\|^2 \\ &+ \boldsymbol{\varrho}^\top \boldsymbol{M}^{-1}(\boldsymbol{\tau} - \hat{\boldsymbol{\tau}}) + \|\mathfrak{n}\|\bar{\xi}\end{aligned} \tag{35}$$

with α_1, α_2 given in (31a). By designing:

$$\boldsymbol{\tau} - \hat{\boldsymbol{\tau}} = -\sigma\boldsymbol{\varrho} = -k\sigma(\boldsymbol{e} - \hat{\boldsymbol{e}}) - \sigma(\boldsymbol{v} - \hat{\boldsymbol{v}}),$$

which is compatible with (30), we get:

$$\begin{aligned}\dot{\Lambda}(\mathfrak{n}) &\leq -\left(\underline{k} - \frac{\alpha_1}{4\varpi}\right)\|\boldsymbol{\rho}_e\|^2 + (\alpha_1\varpi + \alpha_2)\|\boldsymbol{\varrho}\|^2 \\ &\qquad - \sigma\boldsymbol{\varrho}^\top \boldsymbol{M}^{-1}\boldsymbol{\varrho} + \|\mathfrak{n}\|\bar{\xi} \\ &\leq -\left(\underline{k} - \frac{\alpha_1}{4\varpi}\right)\|\boldsymbol{\rho}_e\|^2 + (\alpha_1\varpi + \alpha_2)\|\boldsymbol{\varrho}\|^2 \\ &\qquad - \sigma\lambda_{\min}(\boldsymbol{M}^{-1})\|\boldsymbol{\varrho}\|^2 + \|\mathfrak{n}\|\bar{\xi} \\ &= -\left(\underline{k} - \frac{\alpha_1}{4\varpi}\right)\|\boldsymbol{\rho}_e\|^2 - \left[\sigma\lambda_{\min}(\boldsymbol{M}^{-1}) - \alpha_1\varpi - \alpha_2\right]\|\boldsymbol{\varrho}\|^2 \\ &\qquad + \|\mathfrak{n}\|\bar{\xi} \\ &= -\varsigma_1\|\boldsymbol{\rho}_e\|^2 - \varsigma_2\|\boldsymbol{\varrho}\|^2 + \|\mathfrak{n}\|\bar{\xi} \\ &\leq -\min\{\varsigma_1, \varsigma_2\}\|\mathfrak{n}\|^2 + \|\mathfrak{n}\|\bar{\xi} \\ &\leq -\|\mathfrak{n}\|\left[\min\{\varsigma_1, \varsigma_2\}\|\mathfrak{n}\| - \bar{\xi}\right],\end{aligned} \tag{36}$$

with ς_1, ς_2 as given in (33). Thus, $\Lambda(\mathfrak{n}) < 0$, when

$$\|\mathfrak{n}\| > \frac{\widetilde{\xi}}{\min\{\varsigma_1, \varsigma_2\}}.$$

Taking the latter into consideration and the fact that $\mathfrak{n}(0) = 0$, it holds that:

$$\|\mathfrak{n}(t)\| \leq \frac{\widetilde{\xi}}{\min\{\varsigma_1, \varsigma_2\}}, \quad \forall t \geq 0.$$

Moreover, the following inequalities hold:

$$\|\boldsymbol{\rho}_e\| \leq \|\mathfrak{n}\| \Rightarrow \|\boldsymbol{\rho}_e(t)\| \leq \frac{\bar{\xi}}{\min\{\varsigma_1, \varsigma_2\}}, \quad \forall t \geq 0,$$

$$\left|\|\boldsymbol{\rho}_v\| - k\|\boldsymbol{\rho}_e\|\right| \leq \|\boldsymbol{\rho}_v + k\boldsymbol{\rho}_e\| = \|\boldsymbol{\varrho}\| \leq \|\mathfrak{n}\|$$

$$\Rightarrow \|\boldsymbol{\rho}_v(t)\| \leq \frac{(1+k)\bar{\xi}}{\min\{\varsigma_1, \varsigma_2\}}, \quad \forall t \geq 0.$$

which concludes the proof. ■

A graphical illustration of the proposed tube based control strategy is given in Fig 5. Under the proposed control scheme (22), the real trajectory $\boldsymbol{e}(t)$ lies inside the tube which is centered along the nominal trajectory $\hat{\boldsymbol{e}}$ with radius $\widetilde{\rho}_e$ for all times, i.e., $\|\boldsymbol{\rho}_e(t)\| \leq \widetilde{\rho}_e$, $\forall t \in \mathbb{R}_{\geq 0}$.

C. Bounds on the Unactuated Velocity v

In the sequel, we will prove the boundedness of the unactuated velocity v along the sway direction. Let us define the positive definite and radially unbounded function $V_v = \frac{1}{2}m_{22}v^2$ where m_{22} denotes the vehicle's mass/added-mass of inertia of the sway degree of freedom, see (1f). Differentiating V_v with respect to time and substituting (1f), we obtain:

$$\begin{aligned}\dot{V}_v &= m_{22}v\dot{v} \\ &= -m_{11}uvr + Y_v v^2 + Y_{v|v|}v^2|v| + vm_{22}\delta_Y\end{aligned}$$

which after algebraic manipulations, and using the facts $Y_v, Y_{v|v|} < 0$, $|\delta_Y| \leq \bar{\delta}_Y$, leads to:

$$\dot{V}_v \leq Y_{v|v|}|v|^3 + Y_v|v|^2 + m_{11}\bar{u}\bar{r}|v| + m_{22}\bar{\delta}_Y|v|$$

Therefore, we conclude that $\dot{V}_v$ is negative when

$$|v| > \sqrt{\mathfrak{a} + \mathfrak{b}} + \mathfrak{c}$$

where $\mathfrak{a} \triangleq \left(\frac{Y_v}{2Y_{v|v|}}\right)^2$, $\mathfrak{b} \triangleq \frac{m_{11}\bar{u}\bar{r} + m_{22}\bar{\delta}_Y}{-Y_{v|v|}}$ and $\mathfrak{c} \triangleq -\frac{Y_v}{2Y_{v|v|}}$. Consequently we have:

$$|v(t)| \leq \bar{v} := \max\left\{|v(0)|, \frac{\sqrt{\mathfrak{a} + \mathfrak{b}} - \mathfrak{c}}{m_{22}}\right\}, \ \forall t \geq 0 \tag{37}$$

which intuitively means that for any underactauted underwater vehicle, and for any bounded velocities $|u| \leq \bar{u}$, $|w| \leq \bar{w}$ and $|r| \leq \bar{r}$, the velocity v in the unactuated sway direction remain bounded by an upper bound which depends on: i) the upper bounds $\bar{u}$, $\bar{w}$ and $\bar{r}$, ii) the parameters of the dynamic model (1) and iii) the magnitude of the external disturbances. In a similar way, by defining a positive definite and radially unbounded function $V_{\hat{v}} = \frac{1}{2}m_{22}\hat{v}^2$, we can calculate an upper bound for the nominal velocity $\hat{v}$ given as:

$$|\hat{v}(t)| \leq \hat{\bar{v}} := \max\left\{|\hat{v}(0)|, \frac{\sqrt{\mathfrak{a} + \hat{\mathfrak{b}}} - \mathfrak{c}}{m_{22}}\right\}, \ \forall t \tag{38}$$

where $\hat{\mathfrak{b}} \triangleq \frac{m_{11}\bar{u}\bar{r}}{-Y_{v|v|}}$.

D. Online Optimal Control

As mentioned before, the control action $\hat{\boldsymbol{\tau}}(\hat{\boldsymbol{e}}, \hat{\boldsymbol{v}})$ in eq. (22) will be the outcome of a FHOCP solved for the nominal dynamics eq. (21). In this respect, consider a sequence of sampling times $\{t_k\}$, $k \in \mathbb{N}$, with a constant sampling period $0 < \mathfrak{t} < N$, where N is a prediction horizon such that

$t_{k+1} := t_k + \mathfrak{t}$, $\forall k \in \mathbb{N}$. At each sampling time t_k, a FHOCP is solved as follows:

$$\min_{\hat{\boldsymbol{\tau}}(\cdot)} \left\{ \|\hat{\boldsymbol{e}}(t_k+N)\|_P^2 + \int_{t_k}^{t_k+N} \Big[\|\hat{\boldsymbol{e}}(\mathfrak{s})\|_Q^2 + \|\hat{\boldsymbol{\tau}}(\mathfrak{s})\|_R^2 \Big] d\mathfrak{s} \right\} \quad (39a)$$

subject to:

$$\dot{\hat{\boldsymbol{\chi}}}(\mathfrak{s}) = g(\boldsymbol{\chi}(\mathfrak{s}), \hat{\boldsymbol{\tau}}(\mathfrak{s})), \quad \hat{\boldsymbol{\chi}}(t_k) = \boldsymbol{\chi}(t_k), \quad (39b)$$

$$\hat{\boldsymbol{\chi}}(\mathfrak{s}) \in \widetilde{\mathcal{E}} \times \widetilde{\mathcal{V}}, \hat{\boldsymbol{\tau}}(\mathfrak{s}) \in \widetilde{T}, \quad \forall \mathfrak{s} \in [t_k, t_k+N], \quad (39c)$$

$$\hat{\boldsymbol{\chi}}(t_k+N) \in \mathcal{F}, \quad (39d)$$

where:

$$\boldsymbol{\chi} := [\boldsymbol{e}^\top, \boldsymbol{v}^\top, v]^\top \in \mathbb{R}^6,$$

$$g(\boldsymbol{\chi}, \boldsymbol{\tau}) := \begin{bmatrix} J(\hat{\boldsymbol{e}}, \boldsymbol{p}_d)\hat{\boldsymbol{v}} + \zeta(\hat{\boldsymbol{e}}, \dot{\boldsymbol{p}}_d) + \xi(\hat{\boldsymbol{e}}, \hat{v}) \\ \boldsymbol{M}^{-1}\Big(\hat{\boldsymbol{\tau}} + \boldsymbol{C}(\hat{\boldsymbol{v}}, \hat{v})\hat{\boldsymbol{v}} - \boldsymbol{D}(\hat{\boldsymbol{v}})\hat{\boldsymbol{v}} - \boldsymbol{g}\Big) \\ \frac{1}{m_{22}}\big[-m_{11}\hat{u}\hat{r} + Y_v\hat{v} + Y_{v|v|}|\hat{v}|\hat{v}\big] \end{bmatrix},$$

and Q, $P \in \mathbb{R}^{6\times 6}$ and $R \in \mathbb{R}^{3\times 3}$ are positive definite gain matrices. Moreover, $\widetilde{\mathcal{E}}$, $\widetilde{\mathcal{V}}$ and $\mathcal{F}$ are designing sets that are defined in order to guarantee that while the solution of the FHOCP (39a)-(39d) is derived for the nominal dynamics (21), the real trajectory $\boldsymbol{\chi}(t)$ and control inputs $\boldsymbol{\tau}(t)$ satisfy the corresponding state and input constraints. More specifically, the following modifications are performed:

$$\widetilde{\mathcal{E}} := \mathcal{E} \ominus \mathcal{Z}_1, \quad \widetilde{\mathcal{V}} := V \ominus \mathcal{Z}_2, \quad \widetilde{T} := T \ominus \Big[\mathfrak{K} \circ \widetilde{\mathcal{Z}} \Big],$$

where:

$$\mathfrak{K} := \mathrm{diag}\{-k\sigma I_3, -\sigma I_3\}, \quad \widetilde{\mathcal{Z}} := \mathcal{Z}_1 \times \mathcal{Z}_2.$$

This intuitively means that the sets $\mathcal{E}$, V are tightened accordingly, in order to guarantee that while the nominal states $\hat{\boldsymbol{e}}$, $\hat{\boldsymbol{v}}$ and the nominal control input $\hat{\boldsymbol{\tau}}$ are calculated, the corresponding real states $\boldsymbol{e}$, $\boldsymbol{v}$ and real control input $\boldsymbol{\tau}$ satisfy the state and input constraints $\mathcal{E}$, V and T, respectively[2]. Define the *terminal set* by:

$$\mathcal{F} := \big\{ \hat{\boldsymbol{\chi}} \in \widetilde{\mathcal{E}} : \|\hat{\boldsymbol{\chi}}\|_P \le \bar{\epsilon} \big\}, \quad \bar{\epsilon} > 0, \quad (40)$$

which is employed here in order to enforce the stability of the system [33].

Newly Detected Obstacles: as mentioned before, the obstacles within the workspace may be detected online by the vehicle's on–board sensors (e.g., multi–beam imaging or side scan sonar). In such a case, it should be assured that the solution of the FHOCP corresponds to the region that is accessible by the sensing capabilities of the vehicle. This intuitively means that at the time of sampling t_k when solving the FHOCP, any new obstacles have been taken into account by the controller even for the scenario with maximum running speed (i.e., a case when vehicle moves with its maximum speed under maximum disturbances which is tangent to robot's moving direction.). Thus, recalling that $\bar{R}$ denotes the sensing range of the system as already stated in Section-III-B, the prediction horizon is set as follows:

$$N \le \frac{\bar{R}}{\max\{\bar{u}, \bar{w}, \bar{r}\} + \widetilde{\xi}\mathfrak{t}} \quad (41)$$

[2]This constitutes a standard constraints set modification technique adopted in tube-based NMPC frameworks. For more details see [36]).

Algorithm 1 Implementation of feedback control laws $\boldsymbol{\tau}(t)$

Step 1: At time t_k, the current state of the robot (i.e., $\boldsymbol{\eta}(t_k)$, $\boldsymbol{v}(t_k)$) is measured, the errors $e_d(t_k)$, $e_z(t_k)$ and $e_o(t_k)$ of (11)-(13) are designed, and $\boldsymbol{e}(t_k) = \hat{\boldsymbol{e}}(t_k)$ and $\boldsymbol{v}(t_k) = \hat{\boldsymbol{v}}(t_k)$ are set.
Step 2: Based on $(\boldsymbol{e}(t_k), \hat{\boldsymbol{e}}(t_k))$ and $(\boldsymbol{v}(t_k), \hat{\boldsymbol{v}}(t_k))$ solve FHOCP (39a)-(39d) to obtain the nominal control action $\hat{\boldsymbol{\tau}}(t_k)$ and the actual control action $\boldsymbol{\tau}(t_k) = \hat{\boldsymbol{\tau}}(t_k) + \kappa_i(\boldsymbol{e}(t_k), \hat{\boldsymbol{e}}(t_k), \boldsymbol{v}(t_k), \hat{\boldsymbol{v}}(t_k))$.
Step 3: Apply the control $\boldsymbol{\tau}(t_k)$ to the system, during sampling interval $[t_k, t_{k+1})$, where $t_{k+1} = t_k + \mathfrak{t}$.
Step 4: Measure the state of the system at the next time instant t_{k+1}, and set $t_k \leftarrow t_{k+1}$; **Go to Step 1**.

where $\bar{u}, \bar{w}$ and $\bar{r}$ are defined in (7).

Remark 5. *It should be noticed that in a real scenario, AUVs use sonar sensors to obtain knowledge about the environment. The detection range of these sonar sensors (i.e., $\bar{R}$) depends on many factors, including the frequency. Low frequency sonars can detect objects at very long distance, depending on the sound propagation environment. Medium frequency sonars (typically operating between $7.5kHz$ and up to $30kHz$) can detect a object at a multiple nautical miles. On the other hand, high frequency sonars ($> 100kHz$), typically used for underwater inspection can detect smaller objects at a few hundreds meters (i.e., $> 100m$). Thus, in view of* (7)*, in a real scenario the predefined upper bound of the vehicle velocity can be tuned accordingly to the capability sensing range $\tilde{R}$ of the available sonar system (i.e., by selecting lower values for the velocity constraints in* (7)*, with respect to the original given upper bounds.) in order to get a valuable prediction horizon enough for solving the FHOCP* (39a)-(39d)*.*

The pseudo-code description of the proposed real-time control scheme is given in Algorithm-1. Now we are ready to state the main result of this work:

Theorem 1. *Suppose that at time $t = 0$ the FHOCP* (39a)-(39d) *is feasible. Then, the proposed feedback control law* (22)*,* (30)*, renders the closed-loop system Input-to-State stable (ISS) with respect to the disturbances, for every initial condition $\hat{\boldsymbol{\chi}}(0) \in \mathcal{E}$.*

Proof. The proof of the theorem follows similar arguments presented in our previous work [37]. Due to the fact that only the state of the nominal system is used while the FHOCP (39a)-(39d) is solved, the on-line optimization does not depend on the disturbances. The proof of *feasibility*, follows same arguments as in [33], [37][3] which leads to:

$$\boldsymbol{\chi}\big(t_{k+1} + \mathfrak{s}; \hat{\boldsymbol{\tau}}(\cdot), \boldsymbol{\chi}(t_{k+1})\big) \in \mathcal{E} \times \mathcal{V}, \ \forall \mathfrak{s} \in [0, N].$$

By taking the aforementioned into consideration, the feasibility of a solution to the optimization problem at time t_k implies feasibility at all times t_{n+1} with $n > k$. Thus, since at time $t = 0$ a solution is assumed to be feasible, a solution to the

[3]The analytical proof of feasibility is outside the scope of this work and has been omitted.

optimal control problem is feasible for all $t \in \mathbb{R}_{\geq 0}$. Regarding the *convergence analysis*, due to the fact that the sets $\mathcal{Z}_1$, $\mathcal{Z}_2$ are RPI sets, it holds that:

$$\|\boldsymbol{\rho}_e(t)\| \leq \widetilde{\rho}_e, \forall t \geq 0, \tag{42}$$

$$\|\boldsymbol{\rho}_v(t)\| \leq \widetilde{\rho}_v, \forall t \geq 0, \tag{43}$$

where:

$$\widetilde{\rho}_e := \frac{\bar{\xi}}{\min\{\varsigma_1, \varsigma_2\}}, \quad \widetilde{\rho}_v := \frac{(1+k)\bar{\xi}}{\min\{\varsigma_1, \varsigma_2\}}.$$

Since only the nominal system dynamics (21) are used for the online computation of the control actions $\hat{\boldsymbol{\tau}}(\mathfrak{s}) \in \widetilde{\mathcal{T}}$, $\mathfrak{s} \in [t_k, t_k + N]$ through the FHOCP (39a)-(39d), by invoking nominal NMPC stability results found on [33], it can be proven that the NMPC control law $\hat{\boldsymbol{\tau}}$ renders the closed loop trajectories of the nominal system (21) asymptotically ultimated bounded in the sets $\mathcal{F}$ [38]. Then, from [28, Lemma 4.5, p. 150], there exist class $\mathcal{KL}$ functions β_e, β_v such that:

$$\|\hat{\boldsymbol{e}}(t)\| \leq \beta_e(\|\hat{\boldsymbol{e}}(0)\|, t), \ \forall t \in \mathbb{R}_{\geq 0}, \tag{44}$$

$$\|\hat{\boldsymbol{v}}(t)\| \leq \beta_v(\|\hat{\boldsymbol{v}}(0)\|, t), \ \forall t \in \mathbb{R}_{\geq 0}. \tag{45}$$

By combining (23), (42), (43), (44) and (45), we get:

$$\|\boldsymbol{e}(t)\| \leq \beta_e(\|\hat{\boldsymbol{e}}(0)\|, t) + \widetilde{\rho}_e, \ \forall t \in \mathbb{R}_{\geq 0}$$

$$\|\boldsymbol{v}(t)\| \leq \beta_v(\|\hat{\boldsymbol{v}}(0)\|, t) + \widetilde{\rho}_v, \ \forall t \in \mathbb{R}_{\geq 0}$$

Thus, we have shown that the proposed control law (22),(30) renders the closed-loop system ISS with reference to the disturbances $\boldsymbol{\xi}(t) \in \Xi$, for every initial condition $\boldsymbol{x}(0) \in X$, $\boldsymbol{v}(0) \in V$ which leads to the conclusion of the proof. ■

Remark 6. *Regarding the tube's design parameters, by observing* (31)-(33)*, the parameters* $\overline{J}$, $\lambda_{\min}(M^{-1})$, $\lambda_{\min}(J)$ *are initially given. Then, according to the given dynamics and state constraints, the Lipschitz constants* $\mathcal{L}_1, \ldots, \mathcal{L}_6$ *are computed. Then, we tune the parameter gain* $\underline{k} > 0$ *and subsequently, we tune the remaining three control gains* k, ϖ *and* σ *such that the inequalities in* (31a) *are satisfied.*

V. Simulation Results

Real-time simulation have been performed to demonstrate the efficiency of the proposed approach. The simulation environment was designed based on UwSim dynamic simulator [39], a realistic simulation environment developed in the Robot Operating System (ROS) [40] framework with 1 ms time step which is common in a real time operation with an underwater robotic system. The constrained NMPC employed in this work is implemented using the NLopt Optimization library [41].

We conducted an underwater inspection task under external disturbances representing ocean currents and waves. More specifically, two separate scenarios have been considered: i) obstacle free and ii) constrained workspace including obstacles. In particular, obstacle free scenario consists of a pipeline inspection task where the tracking control problem for an underactuated AUV was considered in along a pipeline structure, while in the constrained scenario, the tracking control problem was considered in a workspace including two obstacles where their locations in $x - y$ plane are given by: $\boldsymbol{p}_1 = [-5, \ 5]^\top$ and $\boldsymbol{p}_2 = [7.8, \ -4]^\top$ respectively (see Fig.6).

In both scenarios we considered a unicycle-like underactuated autonomous underwater vehicle where its dynamic parameters are given in Table-I. The capability sensing range and the horizon of the FHOCP are considered as $\bar{R} = 3$ and $N = 10 * \mathfrak{t} = 1.0\,\text{sec}$ respectively. Moreover, The predefined upper bound of the vehicle velocities in (7) are defined as: $\bar{u} = 0.8\frac{m}{s}$, $\bar{v} = 0.04\frac{m}{s}$, $\bar{w} = 0.6\frac{m}{s}$ and $\bar{r} = 0.6\frac{rad}{s}$. Furthermore, each of the three control inputs must obey the following input constraint: $\bar{\tau}_X = 140N$, $\bar{\tau}_Z = 100N$, $\bar{\tau}_N = 60Nm$. The control design parameters were chosen as $\underline{k} = 1.0$, $\varpi = 4.0$ and $k = 5.0$. In both scenarios, the vehicle initially was at rest and was request to track a desired trajectory within the workspace. In addition, in the subsequent simulation study the dynamics of the considered AUV were affected by external disturbances in the form of slowly time varying sea currents acting along X, Y, Z and N axes of the vehicle frame modeled by the corresponding dynamics $\delta_X = 0.2\sin(2\frac{\pi}{15}t)\frac{m}{s}$, $\delta_Y = 0.2\sin(2\frac{\pi}{15}t)\frac{m}{s}$ $\delta_Z = 0.2\cos(2\frac{\pi}{15}t)\frac{m}{s}$ and $\delta_N = 0.2\sin(2\frac{\pi}{15}t)\frac{m}{s}$ (i.e., we set $\bar{\delta} = 0.6$ and $\bar{\delta}_Y = 0.2$). Furthermore, we considered 20% uncertainties on the AUV dynamic parameters (i.e., we set $\bar{\gamma} = 0.2$).

TABLE I: Vehicle dynamic parameter set

m_{11}	m_{22}	m_{33}	m_{44}
21.5	26.5	26.5	8.0
X_u	Y_v	Z_w	N_r
-70.0	-100.0	-100.0	-50.0
$X_{\|u\|u}$	$Y_{\|v\|v}$	$Z_{\|w\|w}$	$N_{\|r\|r}$
-100.0	-200.0	-200.0	-100.0
	W	B	
	$176.6N$	$181.2N$	

A. Obstacle-Free Scenario

The vehicle initially was at rest from the location $\boldsymbol{\eta}(0) = [-15, \ -12, \ 10, \ 0]$ and was requested to track a trajectory along a pipeline structure. The desired trajectory involving line and curved segments was defined by $\boldsymbol{p}_d(t) = [-10 + 0.015 * \pi t, \ 2.5\sin(0.015\pi t), \ 6\cos(0.015\pi t)]^\top$.The results are given in Fig. 7 - Fig. 11 respectively. The trajectory of the system within the workspace is depicted in Fig. 6 and in 3D space in Fig. 7 respectively. It can be seen that the vehicle performs successfully the trajectory tracking task along the pipeline structure. The evolution of the transformed and real error coordinates are shown in Fig. 8 and Fig. 9 respectively. It can be seen that the real errors remain close to zero and the constraint $e_d(t) \geq \epsilon, \ \epsilon = 0.1$ of (19) remain satisfied during the task operation. In Fig. 10 the vehicle velocities are presented and respective constraints are satisfied. Finally, in Fig. 11 the vehicle's thruster inputs are shown. As it can be seen the input constraints are also satisfied.

B. Constrained Scenario

The vehicle initially was at rest from the location $\boldsymbol{\eta}(0) = [-10, \ -8, \ 9, \ 0]$ and was request to track a trajectory along

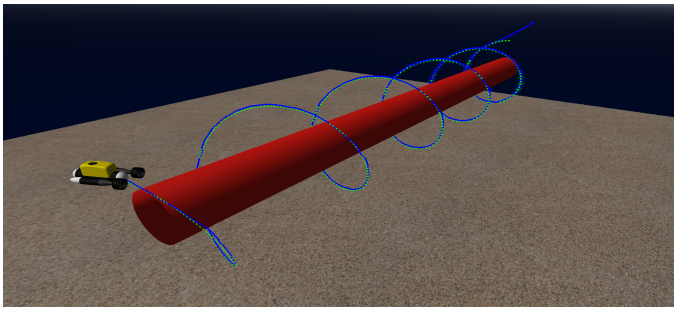

(a) Obstacle free scenario

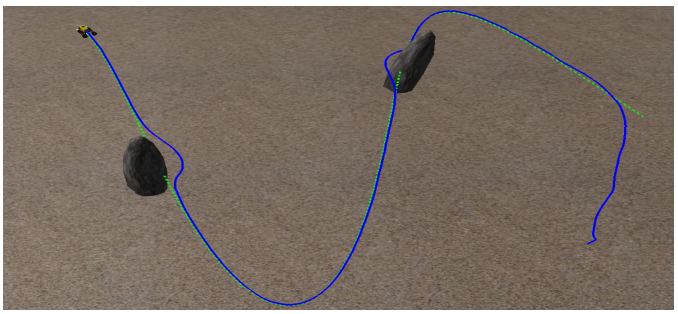

(b) Constrained workspace scenario

Fig. 6: The evolution of the proposed methodology in two separate scenarios: a) obstacle free and b) constrained workspace including obstacles. In obstacle free scenario, an inspection task along a pipeline structure was considered, while in the constrained scenario, the tracking control problem was considered in a workspace including two obstacles. The trace of the vehicle and the desired trajectory are depicted by blue and green lines respectively. The desired trajectory coincides with obstacles positions. The obstacles are detected and considered to the controller when they are within the sensing range $\bar{R}$. The robot has been left the desired trajectory when is needed in order to avoid the obstacles.

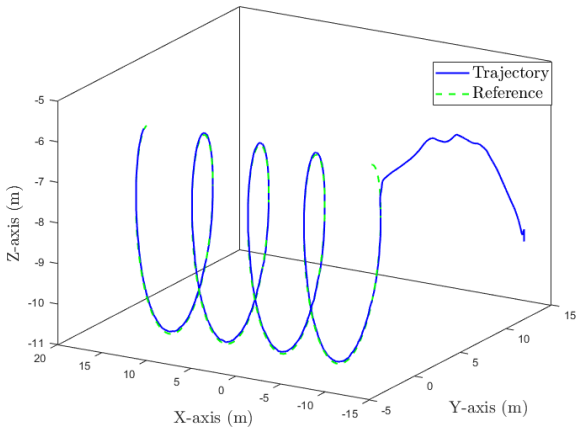

Fig. 7: Obstacle-Free Scenario: The 3D evolution of the vehicle and desired trajectory.

the . The desired trajectory involving line and curved segments was defined by $\boldsymbol{p}_d(t) = [-15+0.1t,\ 12\sin(\frac{\pi}{120}t),\ 8]^\top$. Notice that the desired trajectory that is required to be tracked by the AUV coincides with obstacles positions. The obstacles are modeled according to the spherical world representations as consecutive spheres (i.e., cylinders) with radius $r_{\pi_i} = 0.7m,\ i = \{1, \ldots 2\}$. The radius of the sphere $\mathcal{B}(\boldsymbol{\eta_1}, \tilde{r})$ which

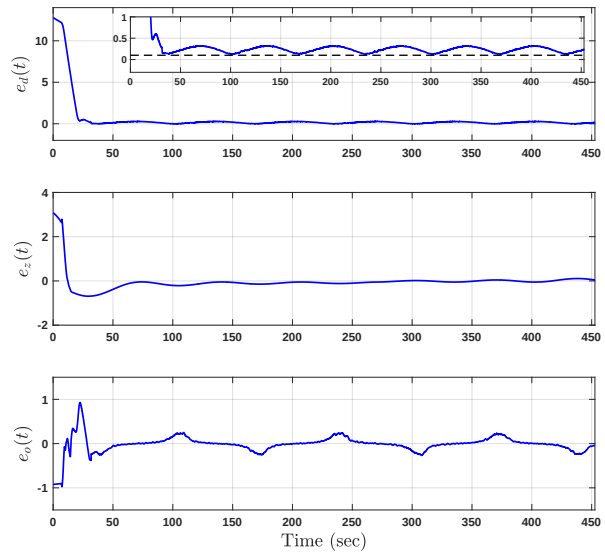

Fig. 8: Obstacle-Free Scenario: The evolution of the transformed errors.

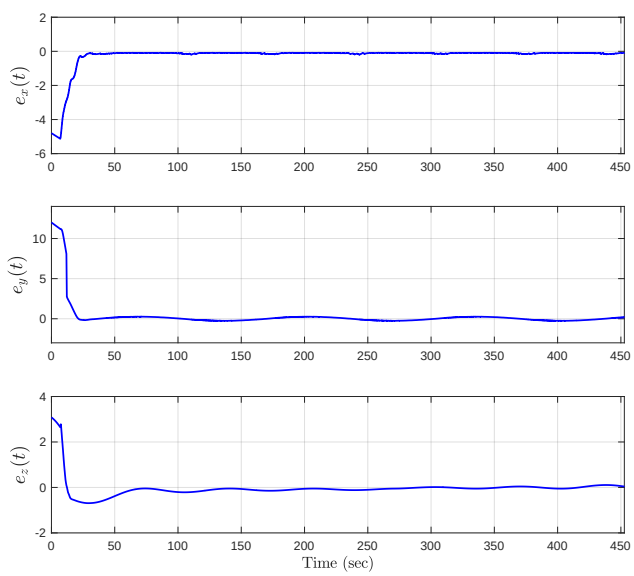

Fig. 9: Obstacle-Free Scenario: The evolution of the real errors.

covers all the vehicle volume (i.e., main body and additional equipment) is defined as $\tilde{r} = 0.4$. However, for the clarity of presentation, we depict it as a safe zone around the obstacles where the vehicle center $\boldsymbol{\eta}_1$ (denoted by blue line, see Fig. 12) should not violated it. The capability sensing range and the horizon of the FHOCP are considered as $\bar{R} = 3$ and $N = 10 * \mathfrak{t} = 1.0\,\text{sec}$ respectively, satisfying the condition (41). Notice that the obstacles are detected and considered by the controller when they are within the sensing range of the robot. Finally, the parameters ϵ_d and ϵ_r defined in (19) are set to $\epsilon_d = 0.1$ and $\epsilon_r = 0.1$.

The simulation scenario has been conducted in such a way that the robot is required to track the desired trajectory which coincides 2 times with obstacles. The results are given in Fig. 12-Fig. 16. The trajectory of the system within the workspace is depicted in Fig. 6 and along horizontal plane in Fig. 12. It can be seen that the vehicle performs successfully the

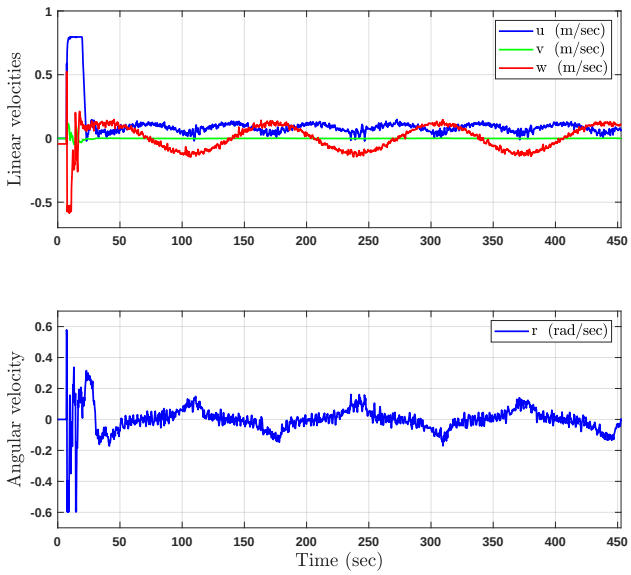

Fig. 10: Obstacle-Free Scenario: The evolution of the vehicle velocities during the task operation.

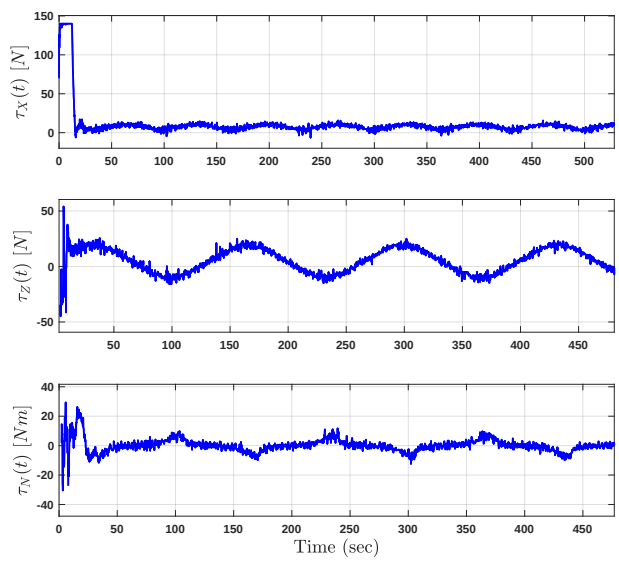

Fig. 11: Obstacle-Free Scenario: The control input signals during the task operation.

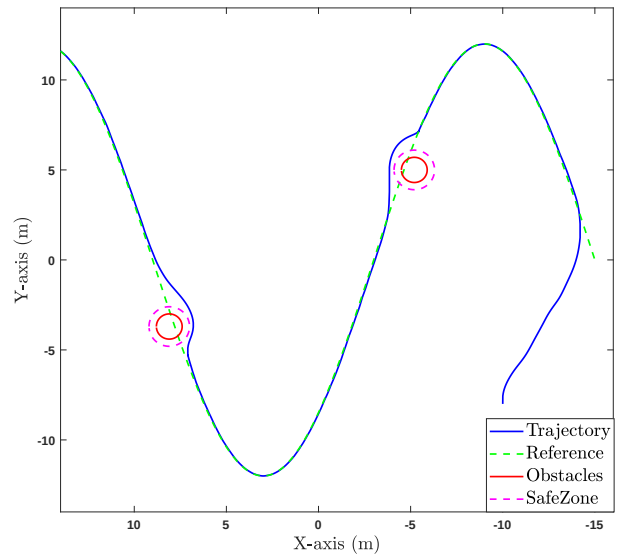

Fig. 12: Constrained Scenario: The evolution of the vehicle and desired trajectory in horizontal plane.

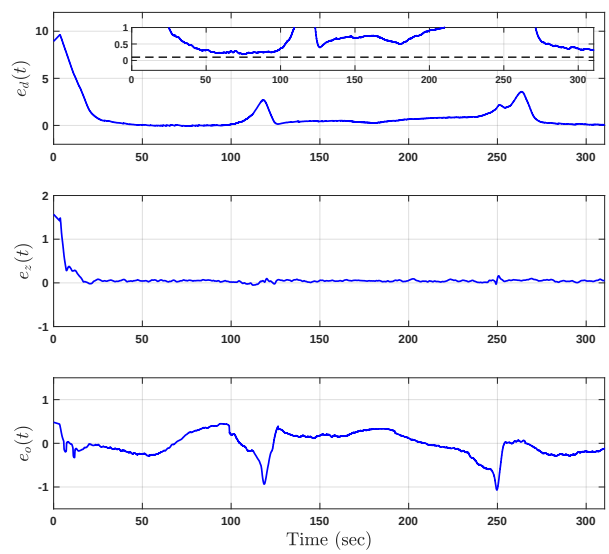

Fig. 13: Constrained Scenario: The evolution of the transformed errors.

trajectory tracking while safely avoids the obstacles within the workspace. We observe that the robot has been left the desired trajectory when it was needed in order to avoid the obstacles. The evolution of the transformed and real error coordinates are shown in Fig. 13 and Fig. 14 respectively. It can be seen that the real errors remain close to zero and the constraint $e_d(t) \geq \epsilon,\ \epsilon = 0.1$ of (19) remain satisfied during the task operation. In Fig. 15 the vehicle velocities are presented and respective constraints are satisfied. Finally, in Fig. 16 the vehicle's thruster inputs are shown. As it can be seen the input constraints are also satisfied.

Video:

A video demonstrating the simulation scenarios of this section can be found in the following link: `https://youtu.be/v-rWqNsCfY0`

VI. Conclusions and Future work

This paper presents a robust trajectory tracking control for underactuated Autonomous Underwater Vehicles operating in a constrained workspace including obstacles. The purpose of the controller is to steer the underactuated AUV on a desired trajectory inside a constrained and dynamic workspace. The workspace knowledge (i.e., obstacles' locations) is constantly updated online via the vehicle's sensors. Obstacle avoidance with any of the detected obstacles is guaranteed, despite the presence of external disturbances. Moreover, various constraints such as: obstacles, workspace boundaries, predefined upper bound of the vehicle velocity (requirements for various underwater tasks such as seabed inspection, mosaicking etc.) are considered during the control design. The proposed feedback control law consists of two parts: i) a Finite Horizon Optimal Control Problem (FHOCP) and ii) a state feedback law which is tuned off-line and guarantees that the real trajectories

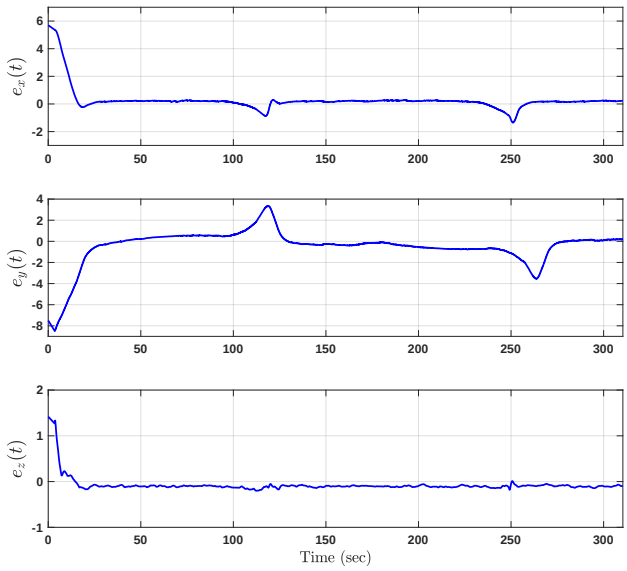

Fig. 14: Constrained Scenario: The evolution of the real errors.

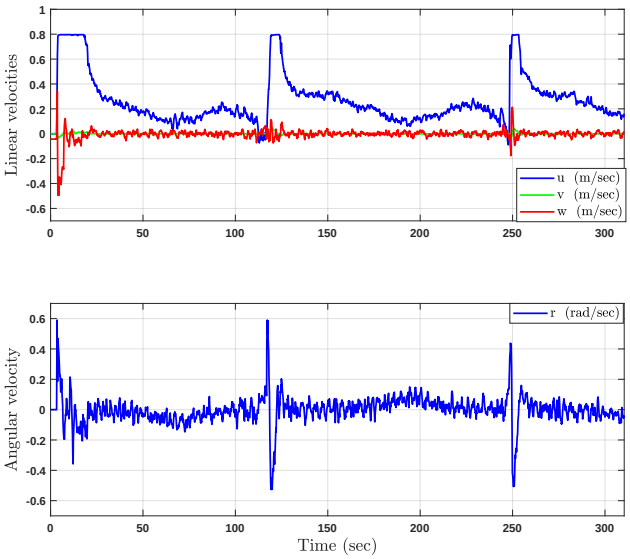

Fig. 15: Constrained Scenario: The evolution of the vehicle velocities during the task operation.

remain inside a tube centered along the nominal trajectories. The closed-loop system has analytically guaranteed stability and convergence properties. Future research efforts will be devoted towards extending the proposed methodology for multiple Autonomous Underwater Vehicles operating in a dynamic environment including not only static but also moving obstacles.

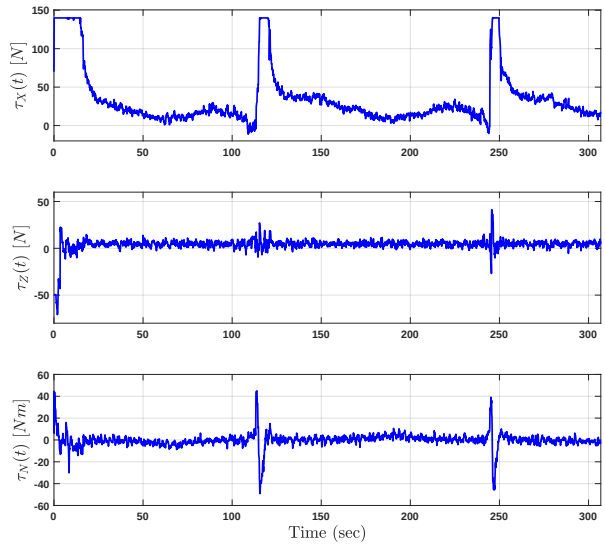

Fig. 16: Constrained Scenario: The control input signals during the task operation.

References

[1] J. Yuh, "Design and control of autonomous underwater robots: A survey," *Autonomous Robots*, vol. 8, no. 1, pp. 7–24, 2000.

[2] X. Xiang, L. Lapierre, and B. Jouvencel, "Smooth transition of auv motion control: From fully-actuated to under-actuated configuration," *Robotics and Autonomous Systems*, vol. 67, pp. 14–22, 2015.

[3] N. Wang, H. R. Karimi, H. Li, and S.-F. Su, "Accurate trajectory tracking of disturbed surface vehicles: A finite-time control approach," *IEEE/ASME Transactions on Mechatronics*, vol. 24, no. 3, pp. 1064–1074, 2019.

[4] T. Fossen, *Handbook of Marine Craft Hydrodynamics and Motion Control*. 2011.

[5] C. Paliotta, E. Lefeber, K. Y. Pettersen, J. Pinto, M. Costa, *et al.*, "Trajectory tracking and path following for underactuated marine vehicles," *IEEE Transactions on Control Systems Technology*, vol. 27, no. 4, pp. 1423–1437, 2018.

[6] Y. Li, C. Wei, Q. Wu, P. Chen, Y. Jiang, and Y. Li, "Study of 3 dimension trajectory tracking of underactuated autonomous underwater vehicle," *Ocean Engineering*, vol. 105, pp. 270–274, 2015.

[7] A. Aguiar and A. Pascoal, "Dynamic positioning and way-point tracking of underactuated auvs in the presence of ocean currents," *International Journal of Control*, vol. 80, no. 7, pp. 1092–1108, 2007.

[8] J. Guerrero, J. Torres, V. Creuze, and A. Chemori, "Trajectory tracking for autonomous underwater vehicle: An adaptive approach," *Ocean Engineering*, vol. 172, pp. 511–522, 2019.

[9] L. Lapierre and B. Jouvencel, "Robust nonlinear path-following control of an auv," *IEEE Journal of Oceanic Engineering*, vol. 33, no. 2, pp. 89–102, 2008.

[10] B. Qiu, G. Wang, Y. Fan, D. Mu, and X. Sun, "Adaptive sliding mode trajectory tracking control for unmanned surface vehicle with modeling uncertainties and input saturation," *Applied Sciences*, vol. 9, no. 6, p. 1240, 2019.

[11] Z. Yan, M. Wang, and J. Xu, "Robust adaptive sliding mode control of underactuated autonomous underwater vehicles with uncertain dynamics," *Ocean Engineering*, vol. 173, pp. 802–809, 2019.

[12] T. Elmokadem, M. Zribi, and K. Youcef-Toumi, "Trajectory tracking sliding mode control of underactuated auvs," *Nonlinear Dynamics*, vol. 84, no. 2, pp. 1079–1091, 2016.

[13] L. Qiao and W. Zhang, "Double-loop integral terminal sliding mode tracking control for uuvs with adaptive dynamic compensation of uncertainties and disturbances," *IEEE Journal of Oceanic Engineering*, vol. 44, no. 1, pp. 29–53, 2018.

[14] N. Wang and M. J. Er, "Self-constructing adaptive robust fuzzy neural tracking control of surface vehicles with uncertainties and unknown disturbances," *IEEE Transactions on Control Systems Technology*, vol. 23, no. 3, pp. 991–1002, 2015.

[15] M. Carreras, J. Yuh, J. Batlle, and P. Ridao, "A behavior-based scheme using reinforcement learning for autonomous underwater vehicles," *IEEE Journal of Oceanic Engineering*, vol. 30, no. 2, pp. 416–427, 2005.

[16] B. Seok Park, "Neural network-based tracking control of underactuated autonomous underwater vehicles with model uncertainties," *Journal of Dynamic Systems, Measurement and Control, Transactions of the ASME*, vol. 137, no. 2, 2015.

[17] B. Patre, P. Londhe, L. Waghmare, and S. Mohan, "Disturbance estimator based non-singular fast fuzzy terminal sliding mode control of an autonomous underwater vehicle," *Ocean Engineering*, vol. 159, pp. 372–387, 2018.

[18] B. Sun, D. Zhu, and S. Yang, "An optimized fuzzy control algorithm for three-dimensional auv path planning," *International Journal of Fuzzy Systems*, vol. 20, no. 2, pp. 597–610, 2018.
[19] C. Bechlioulis, G. Karras, S. Heshmati-Alamdari, and K. Kyriakopoulos, "Trajectory tracking with prescribed performance for underactuated underwater vehicles under model uncertainties and external disturbances," *IEEE Transactions on Control Systems Technology*, vol. 25, no. 2, pp. 429–440, 2017.
[20] S. Heshmati-Alamdari, G. C. Karras, P. Marantos, and K. J. Kyriakopoulos, "A robust predictive control approach for underwater robotic vehicles," *IEEE Transactions on Control Systems Technology*, 2019.
[21] F. Allgöwer, R. Findeisen, and Z. Nagy, "Nonlinear model predictive control: From theory to application," *the Chinese Institute of Chemical Engineers*, vol. 35, no. 3, pp. 299–315, 2004.
[22] C. Shen, Y. Shi, and B. Buckham, "Trajectory tracking control of an autonomous underwater vehicle using lyapunov-based model predictive control," *IEEE Transactions on Industrial Electronics*, vol. 65, no. 7, pp. 5796–5805, 2017.
[23] C. V. Caldwell, D. D. Dunlap, and E. G. Collins, "Motion planning for an autonomous underwater vehicle via sampling based model predictive control," *OCEANS 2010*, pp. 1–6, 2010.
[24] L. V. Steenson, S. R. Turnock, A. B. Phillips, C. Harris, M. E. Furlong, E. Rogers, L. Wang, K. Bodles, and D. W. Evans, "Model predictive control of a hybrid autonomous underwater vehicle with experimental verification," *Proceedings of the Institution of Mechanical Engineers, Part M: Journal of Engineering for the Maritime Environment*, vol. 228, no. 2, pp. 166–179, 2014.
[25] C. Shen, B. Buckham, and Y. Shi, "Modified c/gmres algorithm for fast nonlinear model predictive tracking control of auvs," *IEEE Transactions on Control Systems Technology*, vol. 25, no. 5, pp. 1896–1904, 2016.
[26] C. Petres, Y. Pailhas, P. Patron, Y. Petillot, J. Evans, and D. Lane, "Path planning for autonomous underwater vehicles," *IEEE Transactions on Robotics*, vol. 23, no. 2, pp. 331–341, 2007.
[27] D. N. Subramani and P. F. Lermusiaux, "Energy-optimal path planning by stochastic dynamically orthogonal level-set optimization," *Ocean Modelling*, vol. 100, pp. 57–77, 2016.
[28] H. K. Khalil, "Nonlinear Systems," *Prentice Hall*, 2002.
[29] G. Karras, S. Loizou, and K. Kyriakopoulos, "Towards semi-autonomous operation of under-actuated underwater vehicles: Sensor fusion, on-line identification and visual servo control," *Autonomous Robots*, vol. 31, no. 1, pp. 67–86, 2011.
[30] T. Fossen, "Guidance and control of ocean vehicles," *Wiley, New York*, 1994.
[31] D. Koditschek and E. Rimon, "Robot navigation functions on manifolds with boundary," *Advances in Applied Mathematics*, vol. 11, no. 4, pp. 412–442, 1990.
[32] H. Michalska and D. Mayne, "Robust Receding Horizon Control of Constrained Nonlinear Systems," *IEEE Transactions on Automatic Control (TAC)*, vol. 38, no. 11, pp. 1623–1633, 1993.
[33] H. Chen and F. Allgöwer, "A Quasi-Infinite Horizon Nonlinear Model Predictive Control Scheme with Guaranteed Stability," *Automatica*, vol. 34, no. 10, pp. 1205–1217, 1998.
[34] D. Mayne, J. Rawlings, C. Rao, and P. Scokaert, "Constrained Model Predictive Control: Stability and Optimality," *Automatica*, vol. 36, no. 6, pp. 789–814, 2000.
[35] L. Grüne and J. Pannek, "Nonlinear model predictive control: Theory and algorithms," *Communications and Control Engineering*, 2011.
[36] S. Yu, C. Maier, H. Chen, and F. Allgöwer, "Tube MPC Scheme Based on Robust Control Invariant Set with Application to Lipschitz Nonlinear Systems," *Systems and Control Letters*, vol. 62, no. 2, pp. 194–200, 2013.
[37] A. Nikou and D. V. Dimarogonas, "Decentralized tube-based model predictive control of uncertain nonlinear multiagent systems," *International Journal of Robust and Nonlinear Control*, 2018.
[38] S. Yu, C. Maier, H. Chen, and F. Allgöwer, "Tube mpc scheme based on robust control invariant set with application to lipschitz nonlinear systems," *Systems & Control Letters*, vol. 62, no. 2, pp. 194–200, 2013.
[39] M. Prats, J. Perez, J. Fernandez, and P. Sanz, "An open source tool for simulation and supervision of underwater intervention missions," in *IEEE/RSJ International Conference on Intelligent Robots and Systems (IROS)*, pp. 2577–2582, 2012.
[40] M. Quigley, K. Conley, B. P. Gerkey, J. Faust, T. Foote, J. Leibs, R. Wheeler, and A. Y. Ng, "Ros: an open-source robot operating system," *ICRA Workshop on Open Source Software*, 2009.
[41] S. G. Johnson, "The nlopt nonlinear-optimization package, http://ab-initio.mit.edu/wiki/index.php/nlopt,"

Dr. Shahab Heshmati alamdari received a Diploma in Mechanical Engineering, a Master's Degree in Robotics and Automatic Control and a PhD in Mechanical Engineering from the National Technical University of Athens (NTUA), Athens, Greece, in 2009, 2012, and 2018, respectively. He is currently a Post-Doctoral Researcher with the Division of Decision and Control Systems, School of Electrical Engineering and Computer Science, KTH Royal Institute of Technology, Stockholm, Sweden. His research interests include navigation and sensor based motion planning of unmanned autonomous vehicles (aerial, ground, underwater), reinforcement learning, the task planning and distributed control of multi-robot systems, such as free flying manipulators and autonomous robotic vehicles.

Dr. Alexandros Nikou received the Diploma in Electrical and Computer Engineering in 2012 and the M.Sc. in Automatic Control in 2014, both from National Technical University of Athens (NTUA), Greece. He received his PhD in Electrical Engineering and Computer Science, KTH Royal Institute of Technology, Stockholm, Sweden in 2019. He is currently senior researcher at Ericsson Research AI, Stockholm, Sweden. His current research interests include distributed reinforcement learning and formal methods.

Prof. Dimos Dimarogonas was born in Athens, Greece, in 1978. He received the Diploma in Electrical and Computer Engineering in 2001 and the PhD in Mechanical Engineering in 2007, both from National Technical University of Athens (NTUA), Greece. He has held postdoctoral positions at KTH, Sweden and MIT, USA. He is currently Professor at the Division of Decision and Control, KTH Royal Institute of Technology, Stockholm, Sweden. His current research interests include Multi-Agent Systems, Hybrid Systems and Control, Robot Navigation and Networked Control. He serves in the Editorial Board of Automatica, the IEEE Transactions on Control of Network Systems and is a Senior member of the IEEE.